



Cite this: *Energy Environ. Sci.*, 2025, 18, 4596

## Direct seawater electrolysis for green hydrogen production: electrode designs, cell configurations, and system integrations

Lizhen Wu,<sup>†</sup><sup>a</sup> Yifan Xu,<sup>†</sup><sup>b</sup> Qing Wang,<sup>a</sup> Xiaohong Zou,<sup>a</sup> Zhefei Pan,<sup>\*cd</sup>  
Michael K. H. Leung<sup>†</sup><sup>b</sup> and Liang An<sup>†</sup><sup>ae</sup>

Direct seawater electrolysis (DSE) is a promising technology for sustainable hydrogen production, utilizing abundant marine resources. However, industrialization of DSE faces significant long-term stability challenges due to the complex composition of seawater, which contains various ions and microorganisms that can lead to both chemical and physical degradation of the electrolysis system. For instance, the presence of chloride ions ( $\text{Cl}^-$ ) hinders the desired oxygen evolution reaction (OER) because competing chlorine evolution reactions (CER) occur and adversely impact electrode materials, resulting in low system efficiency and poor longevity. To enhance long-term stability of DSE, researchers are investigating robust electrocatalysts and advanced surface modifications that improve protection against corrosive environments and enhance selectivity. Innovative electrode designs are also being developed to manage bubble transport and decrease precipitation. Additionally, the design of electrolysis cells, such as bipolar membrane cells, offers a viable solution by minimizing  $\text{Cl}^-$  transport and corrosive environment. With an increasing number of offshore renewable energy projects, the integration of effective DSE technologies in the offshore environment is critical. This review provides the state-of-the-art of electrodes, cells and systems, contributing to the development of DSE for long-term stable operation.

Received 24th February 2025,  
Accepted 17th April 2025

DOI: 10.1039/d5ee01093d

rsc.li/ees

### Broader context

Direct seawater electrolysis (DSE) is emerging as a critical technology for sustainable hydrogen production, leveraging the abundant supply of seawater to address global energy demands and reduce reliance on fossil fuels. Despite its potential, the widespread application of DSE faces significant challenges due to the complex chemical composition of seawater, particularly the presence of chloride ions ( $\text{Cl}^-$ ), which can lead to competing reactions like chlorine evolution that degrade the performance of electrocatalysts. Ongoing research focuses on developing robust electrocatalysts, advanced surface modifications, and innovative electrode designs, including novel cell configurations, to enhance the resilience and efficiency of electrolysis systems. As offshore renewable energy projects increase, integrating DSE technologies is vital for sustainable hydrogen production and achieving environmental sustainability goals, paving the way for a more resilient and renewable energy future.

## 1 Introduction

The serious challenges faced globally with increasing energy and environmental risks have prompted a profound shift in the energy mix from traditional fossil energy sources to emerging carbon-free energy alternatives.<sup>1,2</sup> Among these alternatives, hydrogen stands out as a highly promising energy carrier due to its exceptional energy density.<sup>3,4</sup> However, traditional methods for hydrogen production, which rely on fossil fuels, inherently lead to carbon dioxide ( $\text{CO}_2$ ) emissions.<sup>5,6</sup> To mitigate these issues, the production of green hydrogen through water electrolysis powered by renewable energy sources—such as solar and wind—emerges as an ideal solution.<sup>7,8</sup> Existing water electrolysis technologies<sup>9,10</sup>

<sup>a</sup> Department of Mechanical Engineering, The Hong Kong Polytechnic University, Hung Hom, Kowloon, Hong Kong SAR, China. E-mail: liang.an@polyu.edu.hk

<sup>b</sup> Ability R&D Energy Research Centre, School of Energy and Environment, City University of Hong Kong, Kowloon, Hong Kong SAR, China. E-mail: mkh.leung@cityu.edu.hk

<sup>c</sup> Key Laboratory of Low-grade Energy Utilization Technologies and Systems (Chongqing University), Ministry of Education, Chongqing, 400030, China. E-mail: zhefei.pan@cqu.edu.cn

<sup>d</sup> Institute of Engineering Thermophysics, Chongqing University, Chongqing 400030, China

<sup>e</sup> Research Institute for Smart Energy, The Hong Kong Polytechnic University, Hung Hom, Kowloon, Hong Kong SAR, China

† These authors contributed equally to this work.



primarily include alkaline water electrolysis (AWE) and polymer electrolyte membrane (PEM) electrolysis, both of which necessitate high-purity water. This requirement limits their scalability due to the unequal availability and scarcity of freshwater resources.<sup>11</sup> Consequently, seawater, as a virtually unlimited resource, presents a compelling option for seawater electrolysis (SWE).<sup>12</sup> The electrolysis process in seawater involves two half-reactions: the hydrogen evolution reaction (HER) at the cathode<sup>13</sup> and the oxygen evolution reaction (OER) at the anode.<sup>14</sup> While seawater holds considerable promise, its intricate composition presents notable challenges for efficient and sustainable SWE.<sup>11,15</sup>

SWE is generally categorized into two types: indirect seawater electrolysis (ISE) and direct seawater electrolysis (DSE).<sup>16,17</sup> DSE and ISE differ primarily in their pre-treatment requirements. ISE necessitates desalination methods, such as reverse osmosis or electrodialysis, to convert seawater into highly pure water before electrolysis, leading to additional costs and energy losses (up to 7% of the total system cost).<sup>18,19</sup> In contrast, DSE directly utilizes untreated seawater, adding alkaline electrolyte (e.g., 1 M KOH) to suppress the chlorine evolution reaction (CER) and enhance OER.<sup>20</sup> This approach results in alkaline effluent with residual ions (e.g.,  $\text{Cl}^-$ ,  $\text{Mg}^{2+}$ ,  $\text{Ca}^{2+}$ ) and unreacted bases, complicating discharge management. Strategies for managing DSE effluent often involve diluting it with seawater or employing acid and base neutralization. However, these approaches can be detrimental to the marine environment and result in the chemical energy from the neutralization process being released as heat, offering little economic advantage.<sup>21,22</sup> Alternatively, the recirculation systems can filter precipitates (e.g.,  $\text{Mg}(\text{OH})_2$ ,  $\text{Ca}(\text{OH})_2$ ) to minimize waste but require efficient filtration and periodic alkaline replenishment.<sup>23</sup> Resource recovery options exist, such as extracting  $\text{Mg}(\text{OH})_2$  and  $\text{Ca}(\text{OH})_2$  for industrial uses (e.g. construction materials,  $\text{CO}_2$  sequestration)<sup>24</sup> and hypochlorite for disinfection,<sup>25</sup> enhancing process economics. DSE is increasingly favored over ISE due to advancements in electrocatalysis and electrolysis cell design,<sup>26</sup> demonstrating competitive hydrogen production from offshore wind farms at distances over 40–50 km.<sup>27</sup> Moreover, DSE's compatibility with fuel cells enables integrated energy conversion and storage, offering a pathway to harness surplus renewable electricity while providing clean drinking water and renewable energy to arid regions, supporting future energy transitions.<sup>28</sup> However, the industrialization of DSE still faces challenges, particularly concerning catalyst efficiency and system stability, which are critical for large-scale hydrogen production.<sup>29</sup> There exists a considerable body of research focused on three main categories of seawater electrolysis: natural seawater electrolysis (NSE), characterized by a pH of approximately 8.1 and without the addition of strong bases like NaOH or KOH;<sup>11</sup> alkaline seawater electrolysis (ASE), wherein NaOH or KOH is added to adjust the alkalinity of the seawater;<sup>30</sup> and simulated seawater electrolysis (SSE), which typically involves a 0.5 M NaCl solution, potentially modified with NaOH or KOH.<sup>31</sup> Given that above techniques use either untreated seawater or only simple physical pre-treatment (e.g., filtration, disinfection), NSE and ASE can be categorized collectively as DSE. Both DSE and SSE-related research aims to provide valuable technical guidance for DSE.

In recent years, advancements in novel electrode materials,<sup>12,32</sup> electrolysis cells,<sup>33,34</sup> and system design<sup>35,36</sup> have propelled the development of DSE (Fig. 1). The interplay between catalyst activity, stability, and selectivity must be carefully balanced, and various types of electrolysis cells require optimization based on specific electrode and catalyst design criteria.<sup>28</sup> Additionally, optimizing the coupling configurations of renewable energy sources with electrolysis cells and auxiliary machines is crucial for enhancing overall system stability.

In this review, we aim to elucidate the mechanisms underlying the poor stability associated with DSE technologies. We will first provide a detailed overview of the challenges that influence the long-term stability of DSE technologies. Subsequently, we will discuss effective approaches for enhancing the long-term stability of both OER and HER electrodes, encompassing material development, surface modifications, and structural optimization. Furthermore, we will conduct a thorough evaluation of the diverse electrolysis cell designs employed in DSE, including membrane-based and membrane-less configurations, as well as low- and high-temperature electrolysis systems. Additionally, we will analyze stability improvement strategies tailored for SWE systems coupled with intermittent renewable energy sources. Finally, we will summarize the critical stability challenges that require attention in the future development of DSE systems.

## 2 General description and stability challenges of direct seawater electrolysis

DSE is the same as conventional water electrolysis in terms of the main reactions, including OER and HER. However, since seawater is different from acid and alkali solutions as well as pure water, various dissolved ions are present.<sup>43</sup> For example, seawater contains 55 wt%  $\text{Cl}^-$  and 31 wt%  $\text{Na}^+$  by mass,<sup>44</sup> which is the reason why a 0.5 M NaCl solution is usually used as a simulated seawater.<sup>45</sup> Among them,  $\text{Cl}^-$  will undergo CER and compete with OER at the anode, which may form toxic chloride or hypochlorite ions (Fig. 2(a) and (b)).<sup>46,47</sup> Main anions and cations such as  $\text{SO}_4^{2-}$ ,  $\text{Mg}^{2+}$  and  $\text{Ca}^{2+}$  and microbial bacteria/microorganisms are also present.  $\text{Mg}^{2+}$  and  $\text{Ca}^{2+}$  will form  $\text{Mg}(\text{OH})_2$  and  $\text{Ca}(\text{OH})_2$  precipitates (Fig. 2(c)) in environments with locally elevated pH, which occurs at  $\text{pH} \geq \sim 9.5$ , resulting in blockage of the active site, resulting in physical degradation.<sup>48,49</sup> Furthermore, microbial bacteria and microorganisms can contribute to biofouling during seawater electrolysis, also blocking the active sites on the electrodes and the pores of the membrane.<sup>50</sup> It is difficult to avoid issues such chemical and physical/mechanical degradation to cell components of seawater electrolysis,<sup>16</sup> which deteriorates their ability to stabilize for long-term operation. For very small amounts of ions such as  $\text{Br}^-$ ,  $\text{F}^-$ , etc.,<sup>29</sup> they may adsorb onto the electrode surface. In this review, we are not concerned with them because of their low amount.



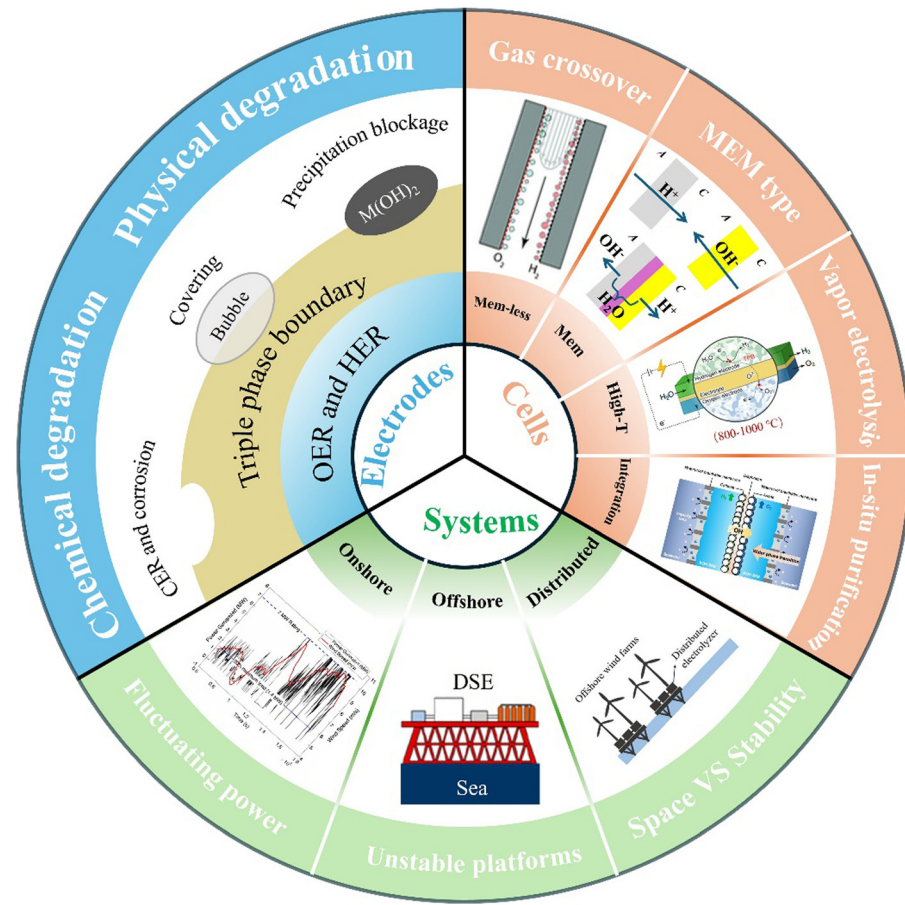
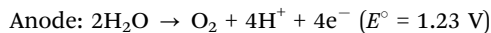


Fig. 1 Possible challenges about long-term stability in DSE. Reproduced with permission.<sup>37</sup> Copyright 2015, The Royal Society of Chemistry. Reproduced with permission.<sup>38</sup> Copyright 2024, American Chemical Society. Reproduced with permission.<sup>39</sup> Copyright 2024, Springer Nature. Reproduced with permission.<sup>40</sup> Copyright 2024, Elsevier. Reproduced with permission.<sup>41</sup> Copyright 2019, American Chemical Society. Reproduced with permission.<sup>42</sup> Copyright 2023, ASME.

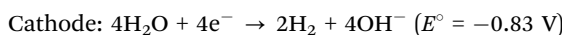
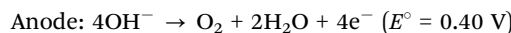
## 2.1 Working principle

The reaction mechanism of DSE is analogous to electrolysis technologies using pure water, the main reaction is  $2\text{H}_2\text{O} \rightarrow 2\text{H}_2 + \text{O}_2$  with the production of oxygen and hydrogen from water, and the cell voltage requires a standard thermodynamic potential of 1.23 V.<sup>44,52</sup> Actually, a higher external voltage is required to drive the reaction.<sup>32</sup> It specifically consists of two half-reactions, anode oxidation to produce oxygen and cathode reduction to produce hydrogen. Depending on the differences in acidic ( $\text{H}^+$ ) and alkaline ( $\text{OH}^-$ ) electrolyte, the cathodic/anodic half-reactions are as follows.<sup>50,53</sup>

Acidic:

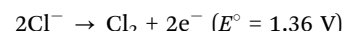


Alkaline:

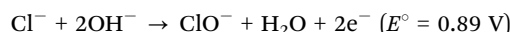


However, due to the complex composition of seawater, challenges associated with DSE including potential side reactions,  $\text{Cl}^-$  ( $\sim 0.54 \text{ M}$ ) plays a major hindering role in the electrolysis process.<sup>54</sup> In the context of the reaction dynamics, the substantial presence of  $\text{Cl}^-$ , paired with the limited availability of  $\text{OH}^-$  and the analogous thermodynamic overpotentials associated with the CER and the OER, positions CER as a formidable side reaction at the anode. Under acidic or alkaline conditions at room temperature, competitive CER are described respectively:<sup>55</sup>

Acidic:



Alkaline:



It is important to highlight that, according to thermodynamics, the OER is somewhat superior to the CER across a generalized pH range.<sup>28</sup> Dionigi *et al.*<sup>46</sup> conducted an in-depth analysis of Pourbaix plots that incorporated chloride and oxygen chemistry (Fig. 2(a)). They discovered that the potential

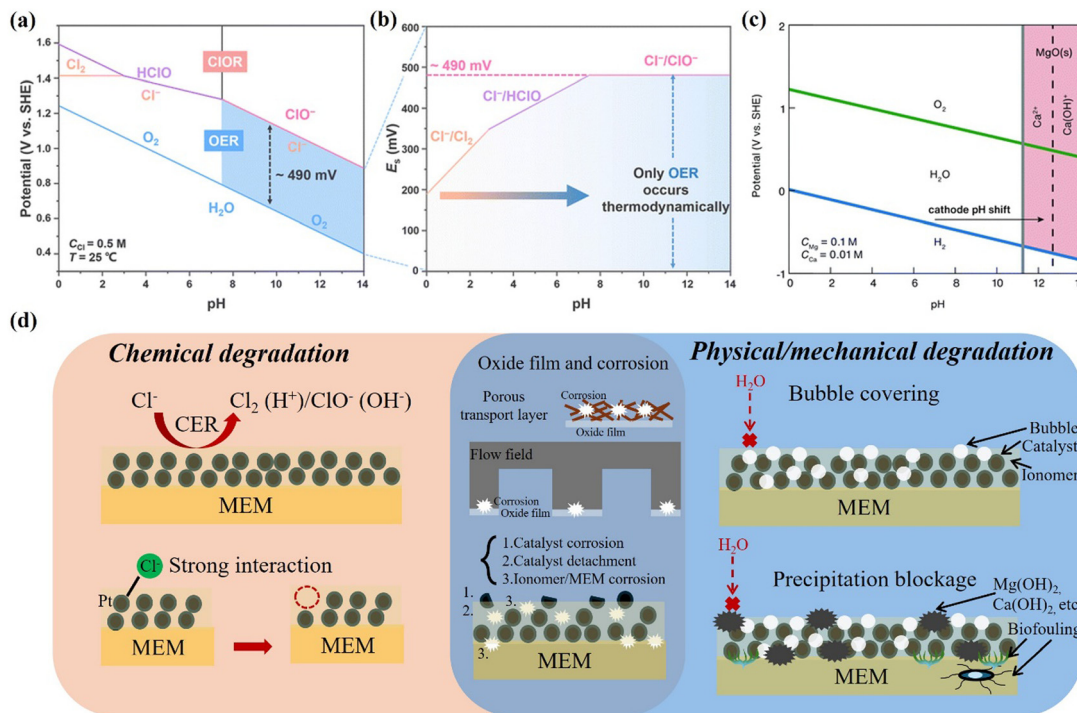


**Fig. 2** (a) The Pourbaix diagram of the DSE. (b) Maximum permitted overpotentials for OER electrocatalysts. Reproduced with permission.<sup>44</sup> Copyright 2024, The Royal Society of Chemistry. (c) Pourbaix diagram of HER and the competitive reduction of impurity cations in seawater. Reproduced with permission.<sup>51</sup> Copyright 2021, The Royal Society of Chemistry. (d) Main long-term stability challenges for DSE: chemical degradation and physical/mechanical degradation.

difference between the CER and the OER is influenced by the pH of the electrolyte. Specifically, at  $\text{pH} < 3$ , the potential difference ranges from 180 to 350 mV, whereas in alkaline conditions ( $\text{pH} > 7.5$ ), this potential difference can reach as high as 490 mV (Fig. 2(b)). This increased potential difference favors the selective occurrence of the OER.<sup>56</sup> However, the kinetics of the four-electron OER is considerably slower than that of the two-electron CER. This disparity leads to significant overpotentials and reduces the thermodynamic advantage of OER, particularly in acidic conditions where the potential gap is at its narrowest.<sup>12</sup> The result indicates that the CER is more advantageous compared to the OER, especially at high current densities. Therefore, based on the alkaline conditions inhibiting CER, alkaline water electrolysis (AWE) cell and anion exchange membrane water electrolysis (AEMWE) cell appear to hold greater promise for DSE compared to proton exchange membrane water electrolysis (PEMWE) cell.<sup>45</sup> In addition, this may be the reason why some of the studies have taken ASE. The primary difference between NSE and ASE is that ASE employs natural seawater as the electrolyte and is supplemented with an alkaline additive (typically 1 M NaOH/KOH), precisely controlling the operating potential of ASE to shift the electrolysis conditions toward those of alkaline water electrolysis, which enhances the competitiveness of  $\text{OH}^-$ .<sup>56</sup> This effectively suppresses the competitive reactions and corrosive effects, thereby significantly improving the durability of electrolyzers. Unlike conventional water electrolysis where only  $\text{H}_2\text{O}$  is consumed, enabling acids and bases to persist within the electrolyzer over

extended operation to maintain required pH conditions (with only periodic replenishment of high-purity water needed), ASE systems face inherent limitations. The continuous replenishment of natural seawater in ASE leads to progressive ion enrichment in the electrolyte. Primarily,  $\text{Ca}^{2+}$  and  $\text{Mg}^{2+}$  ions persistently deplete  $\text{OH}^-$  through precipitation formation, gradually lowering environmental pH and generating difficult-to-remove precipitates.<sup>48,49</sup> Consequently, ASE operation necessitates a flowing electrolyte system with continuous alkaline seawater renewal, posing substantial commercialization challenges—particularly considering that DSE is economically viable mainly when deployed on offshore wind platforms where routine maintenance proves impractical.<sup>35,36</sup> Additionally, the high price of strong alkalis (e.g., \$800 per ton for KOH)<sup>1</sup> is also a barrier to the widespread practical application of ASE. NSE has an undeniable cost advantage in practical applications. We consider that ASE is an improvement of NSE in DSE, and although the cost aspect needs to be improved, all related research aims to provide an effective indirect solution for the lasting development of DSE.

## 2.2 Mechanisms of chemical degradation

DSE is a technology that directly utilizes seawater as the electrolyte, fundamentally falling within the domain of water electrolysis. Consequently, the mechanisms of long-term performance degradation observed in conventional water electrolysis systems also apply to DSE. For instance, the dissolution of anode catalyst materials due to over-oxidation,<sup>57</sup> passivation of

bipolar plates and porous transport layers (PTLs) under high-potential conditions,<sup>3</sup> and degradation of membranes caused by radical attacks and metal ion poisoning,<sup>3</sup> *etc.* However, it is critical to emphasize that the operational environment of DSE is significantly exacerbated by the complex ionic composition of seawater. Compared to alkaline or acidic electrolytes, the lower conductivity of seawater generally results in lower electrolysis efficiency.<sup>58</sup> Moreover, due to the similar overpotentials of OER and CER, seawater electrolysis faces a significant challenge of simultaneously releasing toxic chlorine species at the anode. As we mentioned earlier,  $\text{Cl}_2$  (acidic condition)/ $\text{ClO}^-$  (alkaline condition) produced during the side-reaction CER oxidizes and corrodes the catalyst as well as other key components (Fig. 2(d)) (bipolar plates, porous transport layers, *etc.* are usually made of metal (*e.g.* nickel, titanium or steel) or carbon).<sup>59</sup> The oxide layer of the metal components causes an increase in ohmic loss as the current increases,<sup>60</sup> and the anode potential further increases and exacerbates electrochemical and chemical degradation as described above. For example, the most commonly used catalyst for HER in pure water electrolysis is Pt,<sup>61</sup> but in DSE, the stability of Pt is poor due to the strong interactions between  $\text{Cl}^-$  and Pt preventing the adsorption of the reactants, and ultimately,<sup>62</sup> Pt atoms absorbing large amount of  $\text{Cl}^-$  begin to dissolve (Fig. 2(d)).<sup>63</sup>

### 2.3 Mechanisms of physical/mechanical degradation

Seawater, functioning as a non-buffering agent, causes the pH levels to rise locally at the cathode and fall at the anode during the electrolysis process. The pH near the anode can decrease by roughly 9 units, while at the cathode, it can decrease by roughly 5 units at a current density of  $10 \text{ mA cm}^{-2}$ ,<sup>64</sup> the local pH increase due to the production of  $\text{OH}^-$  by the HER during seawater electrolysis causes the precipitation of metal oxides ( $\text{MgO}$  and  $\text{CaO}$ ) or hydroxides ( $\text{Mg}(\text{OH})_2$  and  $\text{Ca}(\text{OH})_2$ ),<sup>51</sup> which occurs at a pH  $\geq 9.5$ .<sup>65</sup> These insoluble objects not only cover the electrodes and inhibit the mass transfer of  $\text{H}_2\text{O}$ ,<sup>66</sup> resulting in a poor HER stability, but also block other components (*e.g.*, diaphragms or membranes) and cause the membrane dehydration at the cathode, accelerating the chemical degradation of ionomer and membrane (Fig. 2(d)). In addition, for membranes such as AEM, the presence of  $\text{Cl}^-$  can compete with the  $\text{OH}^-$  conductivity of the AEM and increase additional ohmic losses. Increasing the  $\text{OH}^-$  concentration can partially offset the competitive effect,<sup>67</sup> but precipitation formation is also exacerbated. Therefore, this method is not informative and reducing precipitation formation is the more viable option. In addition, there are many organic molecules and micro-organisms in seawater. They are first adsorbed on the surface of electrodes and membrane and then begin to form a conditioning film, providing a basis for microbial attachment. Minutes or hours later, microorganisms such as sulphate-reducing bacteria and algal spores colonize these surfaces by secreting extracellular polymeric substances (EPS) to form biofilms. After that, mature biofilms form multilayered microbial communities.<sup>68</sup> In the coming days or weeks, macroalgae, barnacles, shellfish, and other visible fouling organisms will

attach to the biofilm, creating fouling communities that further promote corrosion and biofouling.<sup>69,70</sup> Biofouling can also block the active sites on the electrodes and the pores of the membrane, showing the obvious physical/mechanical degradation for DSE under long-term operation (Fig. 2(d)).<sup>50</sup> Anti-biofouling measures for membranes and electrodes are not explicitly mentioned in DSE. We can borrow from seawater desalination. Some surface modification techniques are employed, such as hydrophilic coatings like polyethylene glycol (PEG) and polydopamine (PDA) reduce foulant adhesion. PDA-poly(sodium 4-styrene sulfonate) (PSS)/ $\text{TiO}_2$  modified AEMs and PSS&PDA-M membranes exhibit strong fouling resistance.<sup>71</sup> Moreover, the formation and accumulation of gas bubbles generated in response to OER and HER involving gas evolution in water electrolysis usually bring about undesired covering of the active sites causing additional overpotentials.<sup>10</sup> The impact of a large number of bubbles at high currents can also disrupt the interaction between the catalyst and the electrolyte (Fig. 2(d)).<sup>29,72</sup> In addition, due to the complexity of seawater, other degradation phenomena in DSE may introduce unique synergistic mechanisms with bubbles behaviors, which are different from general water electrolysis. For example, compared with fresh water, high salinity reduces the surface tension of seawater and increases the adhesion of bubbles to the electrode, which prolongs the bubble residence time.<sup>73,74</sup> The attachment of bubbles on the electrode surface will hinder the flow of electrolyte and cause a local microenvironment.<sup>75</sup> The anode oxygen bubbles-covered area consumes  $\text{OH}^-$  due to OER, the local pH value of the surrounding area is reduced, and the  $\text{Cl}^-$  concentration increases relatively, which may trigger the CER. When HER occurs at the cathode,  $\text{OH}^-$  is produced and the local pH increases, but the hydrogen bubbles hinder the diffusion of  $\text{OH}^-$ , resulting in the rapid precipitation ( $\text{Mg}(\text{OH})_2$  and  $\text{Ca}(\text{OH})_2$ ) at the edge of the bubble. Therefore, the above degradation constitutes a major challenge and bottleneck for the long-term stability of DSE and is the reason why the long-term durability of DSE (NSE and ASE) is poorer than that of SSE.

## 3 Electrode materials and designs for securing long-term stability

Most DSE electrode designs focus on activity and selectivity, but the low stability due to degradation (seawater-induced degradation such as corrosion and blockage, *etc.* and degradation common to pure water electrolysis such as catalyst detachment, agglomeration and bubble blockage, *etc.*) also needs to be overcome for DSE. However, highly stable materials sometimes limit their activity, so catalytic activity and stability should be balanced during the design of DSE catalysts.<sup>28</sup> The stability of the electrodes can be improved by optimizing the electrode materials to enhance their chemical degradation resistance, by surface modification to improve the selectivity of the OER and HER electrodes in the DSE, and by structural design to rapidly discharge bubbles and improve the formation and distribution of precipitates (Table 1).



**Table 1** The long-term stability for DSE (NSE and ASE) and SSE of recently reported OER and HER catalysts

Catalysts	Electrolyte	$j$ [mA cm <sup>-2</sup> ]	$\eta$ [mV]	Stability	Ref.
OER					
NSE					
Cr <sub>2</sub> O <sub>3</sub> –CoO <sub>x</sub>	Seawater	400	760	230 h@160 mA cm <sup>-2</sup>	76
Mo <sub>3</sub> Se <sub>4</sub> –NiSe	Seawater	10	166	50 h@500 mA cm <sup>-2</sup>	77
PtPd–Ti	Seawater	130	600	12 h@2.0 V (vs. RHE)	78
Zr–Co <sub>3</sub> O <sub>4</sub> /CP	Seawater	100	570	160 h@100 mA cm <sup>-2</sup>	79
CuS@CoOOH	Seawater	10	290	72 h@10 mA cm <sup>-2</sup>	80
HPS–NiMo	Seawater	500	595	120 h@1.8 V (vs. RHE)	81
P/RP-SNCF	Seawater	10	340	100 h@10 mA cm <sup>-2</sup>	82
CoFeOF/nickel foam (NF)	Seawater	100	280	145 h@400 mA cm <sup>-2</sup>	83
ASE					
NiFe/NiS <sub>x</sub> -NF	1.0 M KOH + seawater	400	560	1000 h@400 mA cm <sup>-2</sup>	84
MnCo/NiSe/NF	1.0 M KOH + seawater	1000	460.2	200 h@500 mA cm <sup>-2</sup>	85
CoFe–Ni <sub>x</sub> P/NF	6.0 M KOH + seawater	500	304	600 h@500 mA cm <sup>-2</sup>	86
RuMo <sub>x</sub> /NF	1.0 M KOH + seawater	1000	470	3000 h@500 mA cm <sup>-2</sup>	87
Ru/NiFeOOH	1.0 M KOH + seawater	500	330	400 h@100 mA cm <sup>-2</sup>	88
NiFeO–CeO <sub>2</sub> /NF	1.0 M KOH + seawater	1000	408	200 h@1000 mA cm <sup>-2</sup>	89
Ni <sub>3</sub> S <sub>2</sub> @NiFe LDH/NF	1.0 M KOH + seawater	1000	340	100 h@200 mA cm <sup>-2</sup>	90
NiMoN@NiFeN/NF	1.0 M KOH + seawater	1000	398	100 h@500 mA cm <sup>-2</sup>	91
Fe–Ni <sub>2</sub> P <sub>v–x</sub>	1.0 M KOH + seawater	100	180	100 h@100 mA cm <sup>-2</sup>	92
Co/P–Fe <sub>3</sub> O <sub>4</sub> @IF	1.0 M KOH + seawater	100	290	100 h@500 mA cm <sup>-2</sup>	93
(NiFe)C <sub>2</sub> O <sub>4</sub> /NF	1.0 M KOH + seawater	100	280	600 h@1000 mA cm <sup>-2</sup>	94
NiFe–CuCo LDH	6.0 M KOH + seawater	100	259	500 h@500 mA cm <sup>-2</sup>	95
Fe <sub>2</sub> P/Ni <sub>3</sub> N/NF	1.0 M KOH + seawater	1000	340	40 h@500 mA cm <sup>-2</sup>	96
Ru–Ni(Fe)P <sub>2</sub> /NF	1.0 M KOH + seawater	1000	361	50 h@600 mA cm <sup>-2</sup>	97
Fe <sub>2</sub> P/Ni <sub>1.5</sub> Co <sub>1.5</sub> N/N <sub>2</sub> P	1.0 M KOH + seawater	500	307	40 h@100 mA cm <sup>-2</sup>	98
Ni-doped FeOOH	1.0 M KOH + seawater	200	350	80 h@100 mA cm <sup>-2</sup>	99
Fe–Ni–O–N/NFF	1.0 M KOH + seawater	1000	289	40 h@500 mA cm <sup>-2</sup>	100
S–(Ni,Fe)OOH	1.0 M KOH + seawater	1000	462	100 h@100 mA cm <sup>-2</sup>	101
Ni <sub>2</sub> P–Fe <sub>2</sub> P/NF	1.0 M KOH + seawater	1000	431	48 h@100 mA cm <sup>-2</sup>	102
SSE					
NiFe-LDH/NF	1.0 M NaOH + 0.5 M NaCl	100	270	180 h@400 mA cm <sup>-2</sup>	103
Ir/CoFe-LDH	6.0 M NaOH + 2.8 M NaCl	10	202	1000 h@800 mA cm <sup>-2</sup>	104
Co <sub>3–x</sub> Pd <sub>x</sub> O <sub>4</sub>	1 M PBS + 0.5 M NaCl	10	370	250 h@100 mA cm <sup>-2</sup>	105
Se–NiFe LDH	1.0 M NaOH + 1.0 M NaCl	400	670	600 h@100 mA cm <sup>-2</sup>	106
NiCoHPi@Ni <sub>3</sub> N/NF	1.0 M KOH + 0.5 M NaCl	100	365	120 h@200 mA cm <sup>-2</sup>	107
NiMoFe/NM	1.0 M NaOH + 0.5 M NaCl	100	241	1500 h@100 mA cm <sup>-2</sup>	108
FeCr–Ni <sub>3</sub> S <sub>2</sub>	1.0 M KOH + 0.5 M NaCl	500	286	500 h@500 mA cm <sup>-2</sup>	109
F-NiFe-LDH	1.0 M KOH + 0.5 M NaCl	500	306	1000 h@1000 mA cm <sup>-2</sup>	110
HER					
NSE					
Mo <sub>5</sub> N <sub>6</sub>	Seawater	10	260	100 h@20 mA cm <sup>-2</sup>	111
Co <sub>x</sub> Mo <sub>2–x</sub> C/MXene/NC	Seawater	40	440	225 h@4 mA cm <sup>-2</sup>	63
Pt@mh-3D MXene	Seawater	30	360	250 h@10 mA cm <sup>-2</sup>	112
Ti/NiCo	Seawater	120	1000	10 h@-1.0 V (vs. RHE)	113
PF–NiCoP/NF	Seawater	10	287	20 h@-0.29 V (vs. RHE)	114
Pt <sub>4t</sub> –CoP MNSs/CFC	Seawater	10	300	24 h@10 mA cm <sup>-2</sup>	115
Ni <sub>3</sub> P <sub>4</sub>	Seawater	10	144	10 h@100 mA cm <sup>-2</sup>	116
PtRuMo	Seawater	100	800	20 h@-0.8 V (vs. RHE)	117
CoMoC/Mxene/NC	Seawater	15	500	225 h@-0.5 V (vs. RHE)	63
Pt@mh-3D MXene	Seawater	10	280	250 h@10 mA cm <sup>-2</sup>	112
PtNb–Nb <sub>2</sub> O <sub>5</sub>	Seawater	500	440	360 h@-0.44 V (vs. RHE)	118
Pt/WO <sub>2</sub>	Seawater	10	290	500 h@100 mA cm <sup>-2</sup>	119
ASE					
NiCoP–Cr <sub>2</sub> O <sub>3</sub>	1.0 M NaOH + seawater	4000	275	10 000 h@500 mA cm <sup>-2</sup>	120
F–FeCoP <sub>v</sub> @IF	1.0 M KOH + seawater	1000	210	20 h@100 mA cm <sup>-2</sup>	121
Cu <sub>2</sub> S@NiS@Ni/NiMo	1.0 M KOH + seawater	1000	250	2000 h@500 mA cm <sup>-2</sup>	122
Ru/MoO <sub>2</sub> @NiMoO <sub>4</sub>	1.0 M KOH + seawater	1000	184	50 h@1000 mA cm <sup>-2</sup>	20
Ru/Cd <sub>0.02</sub> Se <sub>4</sub>	1.0 M KOH + seawater	10	6.3	50 h@10 mA cm <sup>-2</sup>	123
Pt–Ni@NiMoN	1.0 M KOH + seawater	10	11	80 h@200 mA cm <sup>-2</sup>	124
Pt–Ni <sub>3</sub> S <sub>2</sub> /Co <sub>9</sub> S <sub>8</sub> –S <sub>v</sub>	1.0 M KOH + seawater	18	10	300 h@100 mA cm <sup>-2</sup>	125
HW–NiMoN-2h	1.0 M KOH + seawater	1000	130	70 h@1000 mA cm <sup>-2</sup>	126
Pt–Ni <sub>3</sub> N@V <sub>2</sub> O <sub>3</sub> /NF	1.0 M KOH + seawater	10	21	500 h@500 mA cm <sup>-2</sup>	127
HPS–NiMo	1.0 M KOH + seawater	10	34	240 h@500 mA cm <sup>-2</sup>	128
Co/P–Fe <sub>3</sub> O <sub>4</sub> @IF	1.0 M KOH + seawater	500	261	100 h@500 mA cm <sup>-2</sup>	76
SA–MoO <sub>2</sub> /Ni <sub>3</sub> (PO <sub>4</sub> ) <sub>2</sub> /NF	1.0 M KOH + seawater	10	46	10 h@100 mA cm <sup>-2</sup>	129
Ni <sub>2</sub> P–Fe <sub>2</sub> P	1.0 M KOH + seawater	1000	389	40 h@500 mA cm <sup>-2</sup>	102
NiMoN@NiFeN	1.0 M KOH + seawater	1000	218	100 h@500 mA cm <sup>-2</sup>	130



Table 1 (continued)

Catalysts	Electrolyte	$j$ [mA cm <sup>-2</sup> ]	$\eta$ [mV]	Stability	Ref.
SSE					
Ni–Co@Fe–Co PBA	1 M KOH + 0.5 M NaCl	183	10	24 h@50 mA cm <sup>-2</sup>	131
NiCoP <sub>v</sub> @NF	1 M KOH + 0.5 M NaCl	1000	237	50 h@100 mA cm <sup>-2</sup>	132
B <sub>x</sub> V-Ni <sub>2</sub> P	1 M KOH + 0.5 M NaCl	100	162	100 h@500 mA cm <sup>-2</sup>	133
NiS–FeS@IF	1 M KOH + 0.5 M NaCl	500	322	500 h@1000 mA cm <sup>-2</sup>	134
Ni–SN@C	1 M KOH + 0.5 M NaCl	10	23	24 h@10 mA cm <sup>-2</sup>	135
a–NiCoS/c–CeO <sub>x</sub>	1 M KOH + 0.5 M NaCl	10	79	50 h@50 mA cm <sup>-2</sup>	136

### 3.1 Electrocatalytic materials and mechanisms for degradation resistance

Rational design of the catalyst composition is an effective way to enhance its corrosion resistance. Mn-based catalysts have been rigorously studied, demonstrating an OER selectivity that exceeds 90% in a 0.5 M NaCl aqueous solution across a range of pH levels.<sup>137</sup> Jiang *et al.*<sup>138</sup> developed a range of MnO<sub>2</sub>-based catalysts incorporating various dual dopants to enhance their

performance as OER catalysts. They found that the inclusion of Fe and V as dopants in  $\gamma$ -MnO<sub>2</sub> effectively strengthened the Mn–O bond and increased corrosion resistance (Fig. 3(a) and (b)). This resulted in the Mn–Fe–V composition exhibiting remarkable stability coupled with a high OER efficiency of 87.96%, maintained over a 500-hour operation period at a current density of 1 A cm<sup>-2</sup> in alkaline NaCl solutions (Fig. 3(c)). Similarly, Ji *et al.*<sup>139</sup> fabricated NiFe layered double hydroxide (LDH)/FeOOH heterostructures

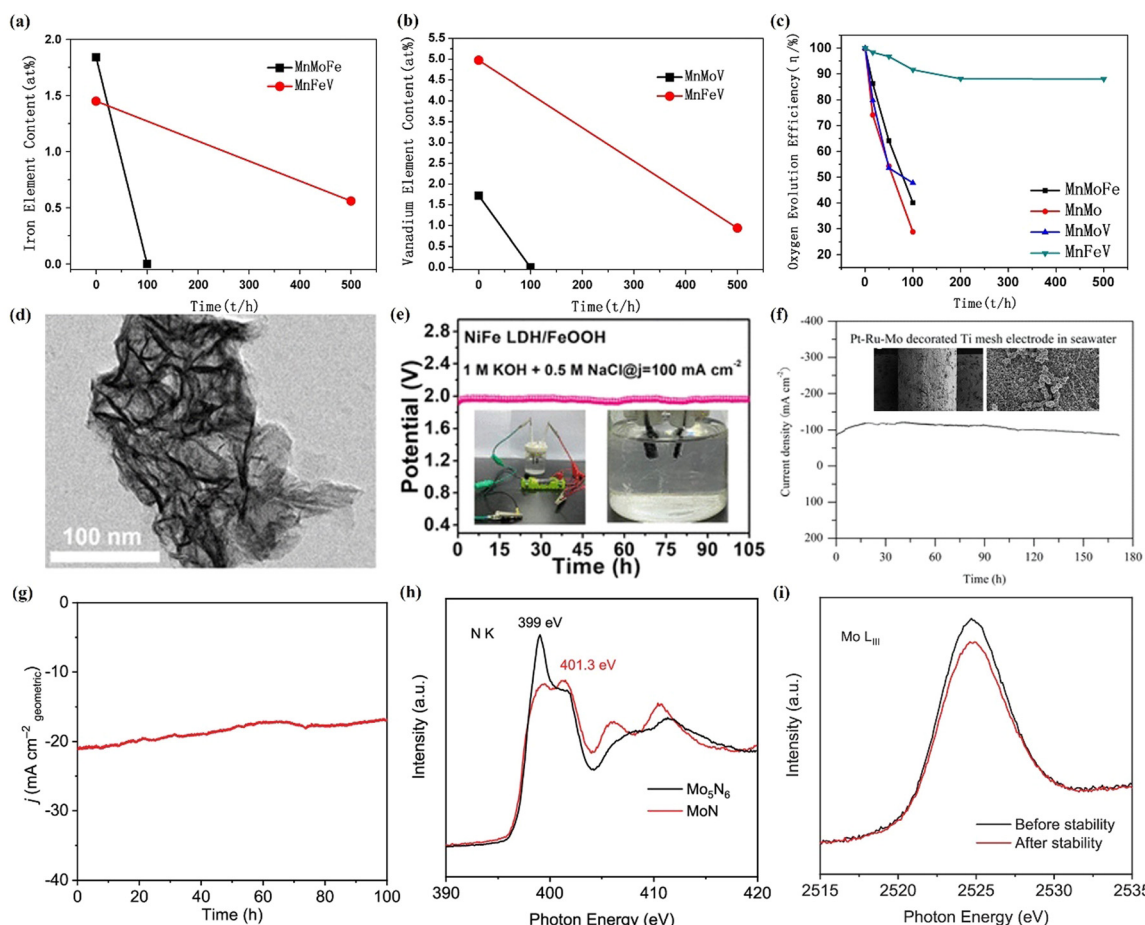


**Fig. 3** The element content changes in the surface oxide compositions of the different elements doped manganese dioxide-coated electrodes before and after electrolysis: (a) Fe and (b) V. (c) The durability of the different elements doped manganese dioxide-coated electrodes. (a)–(c) Reproduced with permission.<sup>138</sup> Copyright 2012, Elsevier. (d) TEM image of the NiFe LDH/FeOOH sample. (e) The durability test of the NiFe LDH/FeOOH in alkaline NaCl solutions. (d) and (e) Reproduced with permission.<sup>139</sup> Copyright 2021, American Chemical Society. (f) The durability test and the SEM images of Pt–Ru–Mo-decorated Ti mesh. Reproduced with permission.<sup>117</sup> Copyright 2021, The Royal Society of Chemistry. (g) The durability test of Mo<sub>5</sub>N<sub>6</sub>. (h) The N K-edge XANES of Mo<sub>5</sub>N<sub>6</sub> and MoN before and after HER. (i) Mo L<sub>III</sub> edge of Mo<sub>5</sub>N<sub>6</sub> before and after HER. Reproduced with permission.<sup>111</sup> (g)–(i) Copyright 2018, American Chemical Society.



deposited on NiFe foam (Fig. 3(d)), achieving strong interfacial interactions. These heterostructures used for overall alkaline simulated seawater splitting with stable operation for 105 hours at a current density of  $100 \text{ mA cm}^{-2}$  (Fig. 3(e)). The enhanced performance was attributed to the heterojunctions, which facilitated the formation of NiOOH species that provided active sites, while the presence of FeOOH contributed significantly to corrosion resistance.

In the field of HER catalyst, alloying platinum-based materials with transition metals such as Fe, Ni, or Mo has been shown to potentially improve their corrosion resistance. Li *et al.*<sup>117</sup> showcased a Pt–Ru–M (where M denotes Cr, Fe, Co, Ni, or Mo) alloy on a titanium mesh, achieving commendable stability exceeding 172 hours for seawater HER (Fig. 3(f)). They elucidated that this enhanced stability was due to the preferential dissolution of the M species over that of Pt and Ru, given that M species were more thermodynamically inclined to dissolve in the presence of corrosive  $\text{Cl}^-$ . Jin *et al.*<sup>111</sup> reported that nitrogen-rich  $\text{Mo}_5\text{N}_6$  exhibits impressive durability, lasting 100 hours at an overpotential of 300 mV in seawater (Fig. 3(g)). The material's structural stability is attributed to its abundant strong metal–nitrogen bonds and the high valence state of molybdenum, which enhances its resistance to detrimental  $\text{Cl}^-$  (Fig. 3(h) and (i)).

### 3.2 Electrode surface modifications

Improving the selectivity of the catalyst is an effective strategy to enhance main reactions and avoid CER side reaction,<sup>140,141</sup> so electrode surface modification is introduced as a more promising and widely adopted approach to increase the OER and HER selectivity.

There are two main ways to carry out the electrode surface modification, including the introduction of other anion ions<sup>84</sup> by electrolyte additives/*in situ* generation and formation of a built-in electric field layer at the electrode–electrolyte interface to repel  $\text{Cl}^-$  and the construction of  $\text{Cl}^-$  a protective layer or blocking layer to decrease the local concentration of  $\text{Cl}^-$  near the electrode. Firstly, Ma *et al.*<sup>103</sup> offered a fresh perspective on surface sulfate additives in enhancing the stability of Ni-based electrodes in DSE. The presence of  $\text{SO}_4^{2-}$  as an additive in the electrolyte tends to be preferentially adsorbed onto the anode surface. This adsorption creates an electrostatic repulsive force that effectively pushes  $\text{Cl}^-$  away from the bulk solution. This repulsive influence of  $\text{SO}_4^{2-}$  is also observed with NiFe LDH nanoarrays on nickel foam anodes, leading to stable performance at a current density of  $400 \text{ mA cm}^{-2}$  over 500 h in real seawater conditions. This stability is reported to be 3 to 5 times greater compared to operations conducted in an electrolyte lacking  $\text{Na}_2\text{SO}_4$ . Fan *et al.*<sup>142</sup> developed a stable earth-rich LDH electrocatalyst for seawater electrolysis, achieving 2800 hours of operation at  $2.0 \text{ V}$  *versus* RHE (Fig. 4(a)). Intercalating carbonate ions and anchoring graphene quantum dots improved corrosion resistance by reducing chloride ion adsorption (Fig. 4(b)). In addition, Liu *et al.*<sup>143</sup> described a cobalt ferricyanide/cobalt phosphide ( $\text{CoFePBA/Co}_2\text{P}$ ) anode that can electrolyze alkaline seawater for more than 1000 hours at  $1000 \text{ mA cm}^{-2}$  (Fig. 4(c))

without corroding due to its self-generated  $\text{PO}_4^{3-}$  and  $\text{Fe}(\text{CN})_6^{3-}$  layers repelling  $\text{Cl}^-$  through electrostatic repulsion during operation (Fig. 4(d)). Tsao *et al.*<sup>106</sup> electrodeposited NiFe LDH onto Se–NiFe foam. During the OER process in alkaline seawater, Se species were *in situ* oxidized to  $\text{SeO}_3^-$  or  $\text{SeO}_4^-$ , which could diffuse into the NiFe LDH layer, effectively repelling  $\text{Cl}^-$  through electrostatic repulsion (Fig. 4(e)). Gong *et al.*<sup>144</sup> developed a NiFe@DG core–shell nanocatalyst with a defective graphene coating that creates a built-in electric field at the electrode–electrolyte interface, repelling corrosive  $\text{Cl}^-$  and protecting active metal sites. The electrolysis cell with NiFe@DG||Pt/C showed excellent performance in seawater with  $1 \text{ M KOH}$ , achieving current densities of  $10 \text{ mA cm}^{-2}$  and  $100 \text{ mA cm}^{-2}$  at low voltages of  $1.496 \text{ V}$  and  $1.602 \text{ V}$ , respectively, while operating stably for 1000 hours (Fig. 4(f)). Zhang *et al.*<sup>145</sup> also created a strong built-in electric field at the  $(\text{Ni}, \text{Fe})\text{OOH}/\text{Ni}_{12}\text{P}_5$  interface, improving oxygen-evolution kinetics while reducing  $\text{Cl}^-$  adsorption.

For the construction of a protective layer or blocking layer, Nocera's research group reports that coatings such as  $\text{Fe}_2\text{O}_3$ ,  $\text{MnO}_2$  and  $\text{PbO}_2$  will help to inhibit  $\text{Cl}^-$ .<sup>147</sup> Wang *et al.*<sup>105</sup> added a  $\text{MnO}_2$  protective layer to nickel foam to prevent  $\text{Cl}^-$  corrosion, then deposited  $\text{Co}_{3-x}\text{Pd}_x\text{O}_4$  on the modified substrate. After 450 hours of continuous operation at  $200 \text{ mA cm}^{-2}$  in natural seawater, the potential remained stable (Fig. 4(g)). Keisuke Obata *et al.*<sup>146</sup> found that a  $\text{CeO}_x$  layer deposited at the anode protects the  $\text{NiFeO}_x$  electrocatalyst from iron loss, ensuring stable performance. This layer permits  $\text{OH}^-$  and  $\text{O}_2$  to pass while blocking  $\text{Cl}^-$ , without impairing the underlying activity of OER catalyst (Fig. 4(h)).

The primary challenges associated with HER electrocatalysts include corrosion resulting from the strong interactions between  $\text{Cl}^-$  and Pt, as well as the precipitation of  $\text{Mg}^{2+}/\text{Ca}^{2+}$  at the cathode, both of which significantly compromise performance and long-term stability. Surface modifications can be employed to mitigate the effects of  $\text{Cl}^-$  corrosion and prevent the precipitation. Xu *et al.*<sup>122</sup> developed a  $\text{Cu}_2\text{S}@\text{NiS}@\text{Ni}/\text{NiMo}$  electrode demonstrating high HER activity with a 250 mV overpotential at  $1000 \text{ mA cm}^{-2}$  and exceptional durability over 2000 h at  $500 \text{ mA cm}^{-2}$  in  $1 \text{ M NaOH}$  and seawater (Fig. 5(a)). The NiS layer provides sulfur for protective polyanion-rich coatings, effectively resisting  $\text{Cl}^-$  corrosion (Fig. 5(b)). Additionally,  $\text{Ni}_3\text{N}@\text{C/NF}$ , featuring  $\text{Ni}_3\text{N}$  nanosheets coated with a carbon shell, protects  $\text{Ni}_3\text{N}$  from poisoning and corrosion by  $\text{Cl}^-$ , achieving the sustained performance over 100 h in  $1 \text{ M KOH}$  and seawater (Fig. 5(c)).<sup>148</sup> For the improvement of precipitation,  $\text{OH}^-$  can be captured or limited, or  $\text{Mg}^{2+}/\text{Ca}^{2+}$  can be repelled from reaching the electrode surface. Guo *et al.*<sup>11</sup> showed that  $\text{OH}^-$  can be captured by an introduced Lewis acid layer (creating a dynamic localized acidic environment) (Fig. 5(d)), such as  $\text{Cr}_2\text{O}_3$ ,  $\text{TiO}_2$  and  $\text{V}_2\text{O}_3$  layer proposed by Hu *et al.*<sup>127</sup> Bao *et al.*<sup>119</sup> exploited the *in situ* formation of hydrotungsten bronze ( $\text{H}_x\text{WO}_y$ ) due to the reversible hydrogen insertion/excretion behavior of  $\text{WO}_2$  to act as a proton 'sponge' to store  $\text{H}^+$  and create an acid-like local environment (Fig. 5(e)), culminating in the proposal of a Pt/ $\text{WO}_2$  catalyst and realizing the long-term



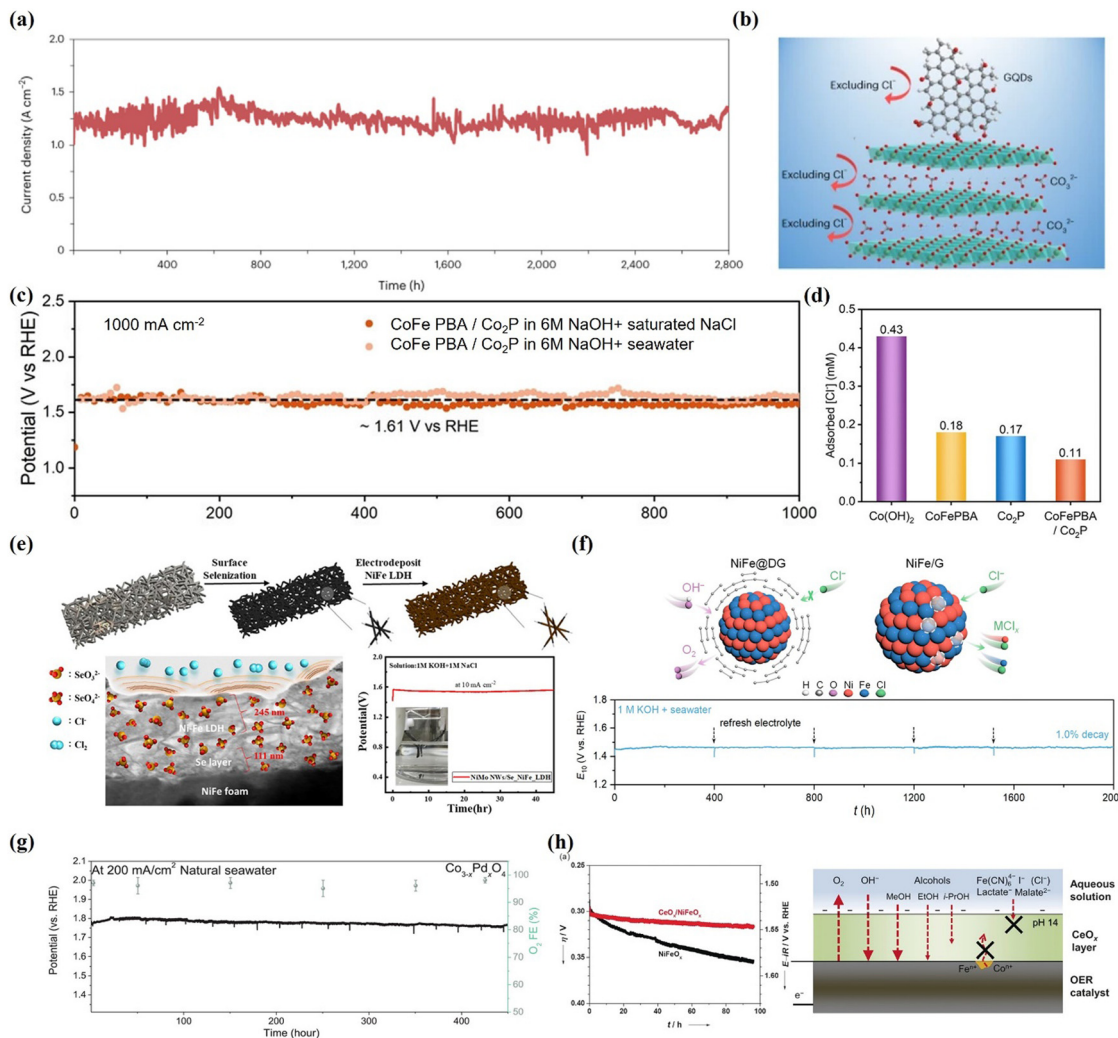


**Fig. 4** (a) Stability test of CoFe–Ci@GQDs/NF at 2.0 V versus RHE in alkaline simulated seawater for 2800 h. (b) Schematic diagram of CoFe–Ci@GQDs protection mechanism against  $\text{Cl}^-$  corrosion in seawater. (a) and (b) Reproduced with permission.<sup>142</sup> Copyright 2024, Springer Nature. (c) Stability test at  $1000 \text{ mA cm}^{-2}$  in electrolytes: 6 M NaOH + saturated NaCl vs. 6 M NaOH + seawater. (d) Adsorbed  $\text{Cl}^-$  quantification on various electrodes in 6 mM NaOH + 2.8 mM NaCl via ion chromatography. (c) and (d) Reproduced with permission.<sup>143</sup> Copyright 2023, Wiley. (e) The mechanism of the improvement of stability of the Se-NiFe-LDH electrode. Reproduced with permission.<sup>106</sup> Copyright 2021, Elsevier. (f) The stability tests and mechanism of enhanced durability for NiFe@DG compared to NiFe/G. Reproduced with permission.<sup>144</sup> Copyright 2023, American Chemical Society. (g) Stability tests of  $\text{Co}_{3-x}\text{Pd}_x\text{O}_4$  catalysts on  $\text{MnO}_2$  protected Ni foam substrates at current densities of  $200 \text{ mA cm}^{-2}$ . Reproduced with permission.<sup>105</sup> Copyright 2023, Wiley. (h) The electrocatalytic stability test at  $20 \text{ mA cm}^{-2}$  and representation of the enhanced stability achieved through the deposition of  $\text{CeO}_x$  on the OER catalyst. Reproduced with permission.<sup>146</sup> Copyright 2018, Wiley.

stability of  $>500$  hours at  $100 \text{ mA cm}^{-2}$  in natural seawater electrolysis (Fig. 5(f)).

### 3.3 Electrode structures and configurations

Firstly, optimizing the electrode structure and configuration can significantly improve its own electrochemical active surface area (ECSA), or activity. Nonetheless, the intrinsic electrochemical activity of electrode is not completely harnessed.<sup>149</sup> In particular, the control of the electrode structure encompasses aspects such as the thickness of the porous structure, the arrangement of catalytic sites, micro- and nano-pore structures and hierarchical pore structures. These factors play a crucial role in modulating the interfacial engineering of mass transport and electron and ion conduction throughout the

reactions at the electrodes<sup>150,151</sup> and in optimizing the effective use of the catalytic sites.<sup>10</sup> Most importantly, it can also improve the unstable operation caused by chemical and physical/mechanical degradation in seawater electrolysis (accumulation of bubbles during OER and HER reactions, precipitation of metal oxides or hydroxides covering the cathode electrodes). This can affect ion transport and corrosion resistance at the interface, as well as interfacial delamination over long periods of operation all further affecting long-term stability.<sup>152</sup>

It was found that a heterogeneous bimetallic phosphide,  $\text{Ni}_2\text{P}-\text{Fe}_2\text{P}$ , on Ni foam is an effective bifunctional catalyst for seawater electrolysis through an *in situ* growth-ion exchange phosphidation method. The resulting porous, ultrathin nanosheets (7.4 nm) exhibited hydrophilic properties (Fig. 6(a)),



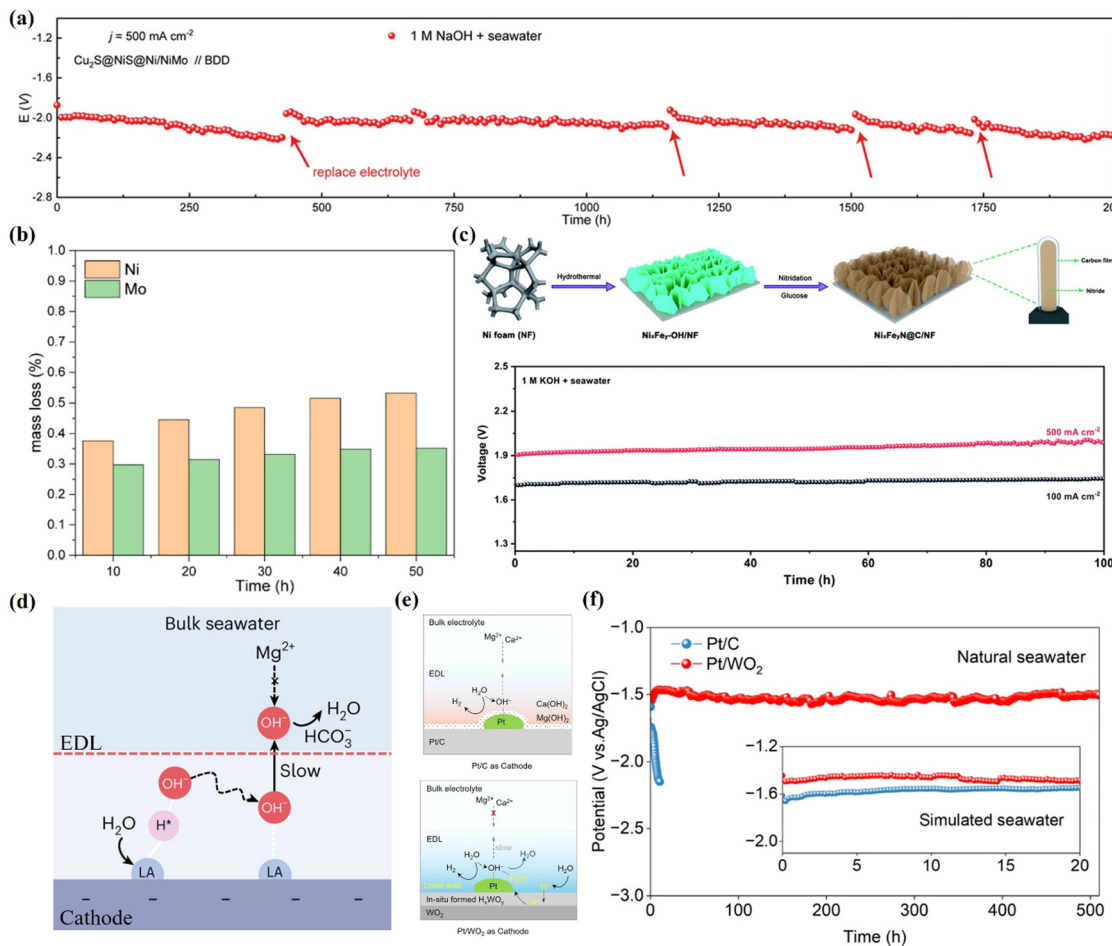


Fig. 5 (a) Stability test of BDD//Cu<sub>2</sub>S@NiS@Ni/NiMo at 500 mA cm<sup>-2</sup> in 1 M NaOH + seawater. (b) Time-dependent mass loss measurement of Cu<sub>2</sub>S@NiS@Ni/NiMo under 400 mA cm<sup>-2</sup>. (a) and (b) Reproduced with permission.<sup>122</sup> Copyright 2023, Wiley. (c) The preparation process of Ni<sub>1-x</sub>Fe<sub>2y</sub>N@C/NF and stability tests at 100 and 500 mA cm<sup>-2</sup>. Reproduced with permission.<sup>148</sup> Copyright 2021, The Royal Society of Chemistry. (d) Schematic illustrating the generation of a local alkaline microenvironment at the Lewis acid-modified cathode, enhancing HER while inhibiting precipitate formation. Reproduced with permission.<sup>11</sup> Copyright 2023, Springer Nature. (e) Schematic comparison of the HER mechanisms on Pt/C and Pt/WO<sub>2</sub>. (f) Stability testing at 100 mA cm<sup>-2</sup> over Pt/WO<sub>2</sub> and Pt/C in natural seawater under Ar. Reproduced with permission.<sup>119</sup> Copyright 2024, American Chemical Society.

enhancing specific surface area (Fig. 6(b)), electrolyte diffusion, and bubble release, which improved the electrocatalyst's stability at high current densities.<sup>102</sup> In addition, a similar function was achieved by the multilayer crystalline-amorphous heterostructured electrode material NF/(CoMo)<sub>0.85</sub>Se@FeOOH proposed by Li *et al.*<sup>153</sup> (Fig. 6(c)), featuring a porous architecture for enhanced active site exposure and mass transfer. This also emphasizes the importance of constructing porous structures and achieving ideal surface superhydrophobicity and superhydrophilicity to ensure adequate exposure to active sites and efficient mass transfer.<sup>154</sup> The multilayered architecture, featuring a (CoMo)<sub>0.85</sub>Se core with a FeOOH shell and an *in situ* formed transition metal (oxy)hydroxide outer layer enriched with polyatomic anions (MoO<sub>x</sub><sup>n-</sup> and SeO<sub>x</sub><sup>n-</sup>), demonstrates excellent mechanical stability and resistance to chloride corrosion in harsh seawater conditions. Liu *et al.*<sup>155</sup> proposed a design, O<sub>s</sub>-Ni<sub>4</sub>Mo/MoO<sub>2</sub> micropillar arrays (Fig. 6(d)) with strong metal-support interaction (MSI), for seawater electrolysis. Strong MSI between O<sub>s</sub> and Ni<sub>4</sub>Mo/MoO<sub>2</sub> enhances the catalyst's

surface electronic structure, lowering the reaction barrier and boosting catalytic activity. In addition, this design not only enhances electron and mass transfer, but also creates a dual Cl<sup>-</sup> repelling layer using electrostatic force to protect active sites from Cl<sup>-</sup> attack in seawater oxidation, consisting of strong O<sub>s</sub>-Cl adsorption and an *in situ*-formed MoO<sub>4</sub><sup>2-</sup> layer. Consequently, it shows excellent stability, with a degradation of just 0.37  $\mu$ V h<sup>-1</sup> after 2500 hours of seawater oxidation. For the precipitation, Liang *et al.*<sup>156</sup> developed a novel honeycomb-like 3D structure with longitudinal micro-channels for a microscopic bubble/precipitate traffic system, allowing for robust anti-precipitation in seawater (Fig. 6(e)). This ordered cathode generates uniform small-sized bubbles that aid in self-cleansing (Fig. 6(e)). Liu *et al.*<sup>157</sup> designed a seawater HER electrode with a Ni(OH)<sub>2</sub> nanofiltration membrane grown on nickel foam at room temperature (Fig. 6(f)). The positively charged Ni(OH)<sub>2</sub> membrane, featuring nanometer-scale cracks, selectively hinders the transfer of Mg<sup>2+</sup>/Ca<sup>2+</sup>, reducing precipitation by 98.3% (Fig. 6(g)). This design ensures rapid transfer of OH<sup>-</sup> and H<sub>2</sub>O

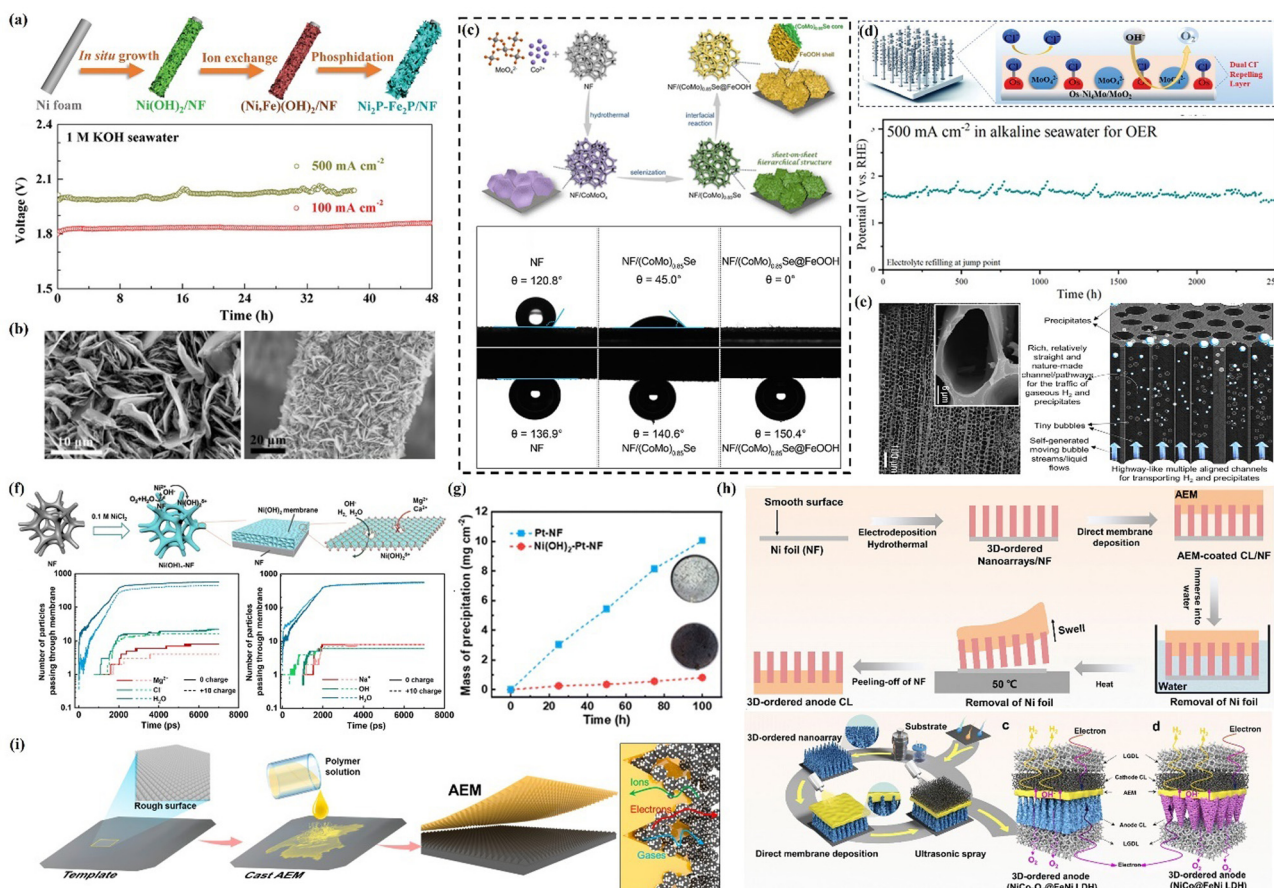


Fig. 6 (a) Schematic illustration of the formation of  $\text{Ni}_2\text{P}-\text{Fe}_2\text{P}/\text{NF}$  and chronopotentiometric curves at 100 and  $500 \text{ mA cm}^{-2}$  for overall water/sweater splitting in 1 M KOH seawater. (b) SEM images of  $\text{Ni}_2\text{P}-\text{Fe}_2\text{P}/\text{NF}$ . (a) and (b) Reproduced with permission.<sup>102</sup> Copyright 2020, Wiley. (c) Synthetic procedure for the  $\text{NF}/(\text{CoMo})_{0.85}\text{Se}@\text{FeOOH}$  nanosheet array and wetting characteristics of bare NF,  $\text{NF}/(\text{CoMo})_{0.85}\text{Se}$ , and  $\text{NF}/(\text{CoMo})_{0.85}\text{Se}@\text{FeOOH}$ . Reproduced with permission.<sup>153</sup> Copyright 2023, American Chemical Society. (d) Schematic illustration of dual  $\text{Cl}^-$  repelling layer and chronopotentiometry curves of  $\text{O}_2-\text{Ni}_4\text{Mo}/\text{MoO}_2$  for OER. Reproduced with permission.<sup>155</sup> Copyright 2024, Wiley. (e) SEM images of the honeycomb-like 3D electrode and its mechanism of repelling precipitation. Reproduced with permission.<sup>156</sup> Copyright 2024, Elsevier. (f) The number of  $\text{Mg}^{2+}$ ,  $\text{Cl}^-$ , and  $\text{H}_2\text{O}$  passing through the charged and uncharged  $\text{Ni}(\text{OH})_2$  nanosheet. (g) The mass of precipitation on the  $\text{Ni}(\text{OH})_2-\text{Pt}-\text{NF}$  and Pt-NF electrodes. Reproduced with permission.<sup>157</sup> Copyright 2023, The Royal Society of Chemistry. (h) Details of the novel swell-assisted transfer method. and schematic illustration of the general fabrication method of the 3D-ordered ACL in an MEA. Reproduced with permission.<sup>158</sup> Copyright 2024, The Royal Society of Chemistry. (i) Preparation of patterned membrane and schematic diagram of membrane electrode with patterned membrane. Reproduced with permission.<sup>159</sup> Copyright 2024, American Chemical Society.

for enhanced HER activity and stability than the Nickel foam electrode. In terms of electrode-membrane interface, Frisch *et al.*<sup>152</sup> adopted a combined catalyst coated membrane (CCM) and catalyst coated substrate (CCS) approach (a lower ( $2 \text{ mg}_{\text{LDH}} \text{ cm}^{-2}$ ) and a higher ( $8 \text{ mg}_{\text{LDH}} \text{ cm}^{-2}$ ) amount on the membrane (CCM) and on the PTL (CCS), respectively.), enhancing catalyst adhesion and reducing delamination at the interface. Since there are fewer studies on the improvement of membrane-electrode interface for DSE, we can draw on the relevant strategies in AEMWE. Wan *et al.*<sup>158</sup> proposed a swelling-assisted transfer strategy to build ordered anode catalyst layers (ACL) on AEM (Fig. 6(h)). Specifically, a three-dimensional interlocked ACL/AEM interface, formed by direct membrane deposition method, can be perfectly transferred to the ordered ACL to AEM, thus permitting vertically orientated through-hole ACL structures and aligned ionic layer layers for  $\text{OH}^-$  transfer. Stable operation was achieved for 700 h in pure

water-feeding mode at  $\sim 1.7 \text{ V}$  with a current density of  $1000 \text{ mA cm}^{-2}$  due to the strong adhesion between the membrane and CL. Hu *et al.*<sup>159</sup> presented an easy method to prepare patterned membranes by casting a polymer solution to the surface of commercially available monocrystalline silicon plates that have a pyramidal pattern on their surface (Fig. 6(i)). The prepared membranes show 39% permeability and 23% enhancement in electrochemical surface area as compared to flat membranes with the same catalyst loadings.

## 4 Electrolysis cell designs for continuous and large-scale production

The electrode referenced earlier plays a crucial role in DSE and has been the subject of numerous studies aimed at enhancing its long-term stability. Challenging seawater environments and



severe operational conditions, such as elevated current densities and high temperatures, impose significant demands on catalyst performance. Regrettably, many existing catalyst engineering approaches fall short of fulfilling the rigorous requirements for practical applications. The design of the reactors and their components also significantly influences overall stability. Additionally, various strategies for improving stability are tied to different electrolyte and reactor configurations. In this section, we will provide a comprehensive description of these aspects.

#### 4.1 Membrane-less electrolysis cells

The most common type of membrane-less electrolysis cell is the single-compartment electrolysis cell, which utilizes a three-electrode system. This design is frequently employed in laboratory-scale catalyst screening experiments.<sup>17</sup> However, there remains a disconnect between the testing conducted with these electrolysis cells and actual production processes, a topic

we will not delve into here. Membrane-less electrolysis cells hold significant promise for DSE due to their streamlined design, which features fewer components compared to membrane electrolysis cells.<sup>30</sup> However, they demand higher catalyst activity and selectivity, making it still in need of further research. For example, macro membrane-less electrolysis cells face challenges like gas crossover,<sup>160</sup> but various methods have been developed to mitigate this issue. One traditional approach utilizes the Segré–Silberberg effect (relies on shear-induced lift to maintain neutrally buoyant particles at a fixed distance from the center in laminar flow), where controlling bubbles around electrodes *via* a flow rate gradient helps separate H<sub>2</sub> and O<sub>2</sub> into distinct effluent channels (Fig. 7(a)).<sup>37</sup> For instance, using two flow-through electrodes made of porous metal mesh positioned face-to-face allows the electrolyte to carry H<sub>2</sub> and O<sub>2</sub> into separate channels (Fig. 7(b)), reducing gas crossover.<sup>161</sup> O’Neil *et al.*<sup>162</sup> tried angling these electrodes and adding insulating plates (Fig. 7(c)), resulting in an increase in ohmic impedance but minimized gas

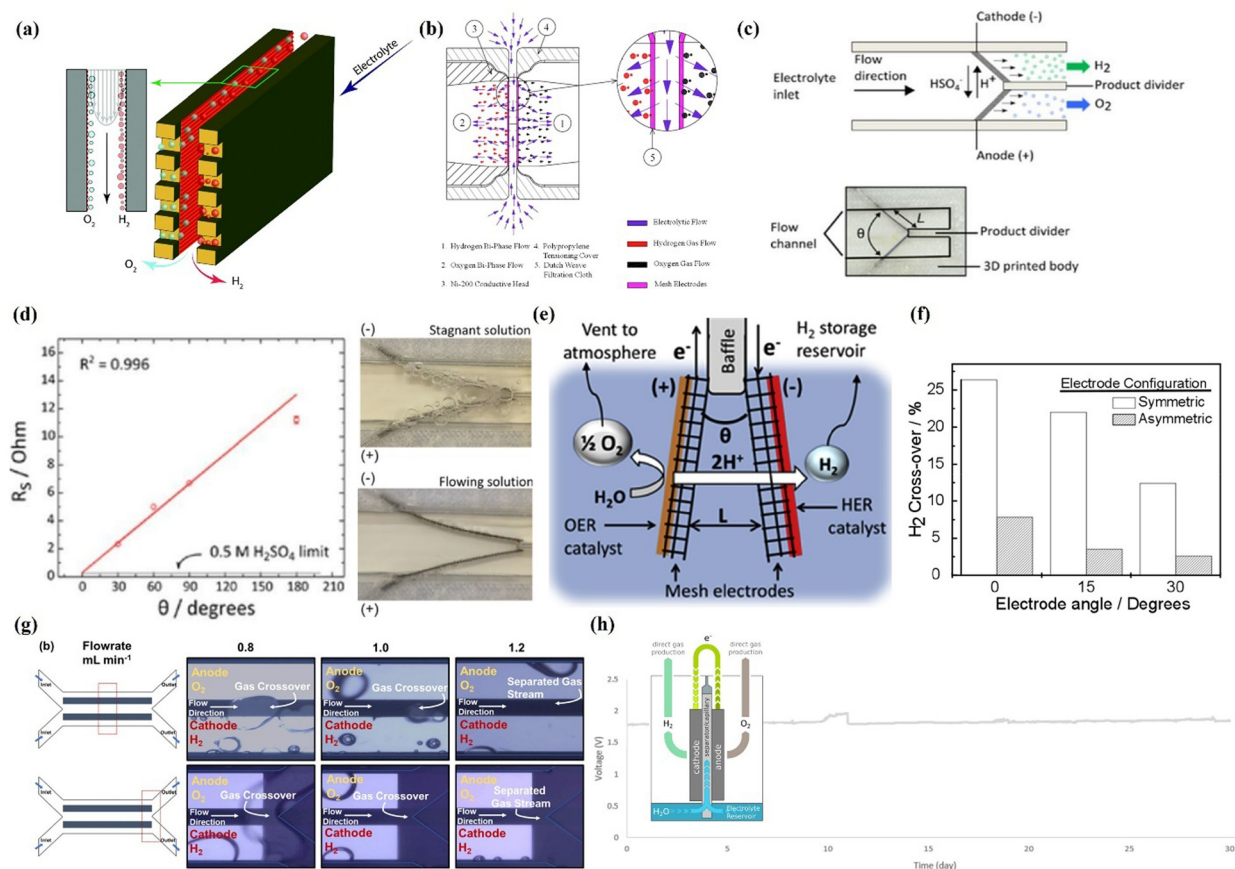


Fig. 7 (a) The membrane-less electrolysis cell separates the produced gas utilizing Segré–Silberberg effect. Reproduced with permission.<sup>37</sup> Copyright 2015, The Royal Society of Chemistry. (b) Mechanism of membrane-free divergent electrode-flow-through electrolysis. Reproduced with permission.<sup>161</sup> Copyright 2015, Elsevier. (c) Membrane-less electrolysis cell utilizing angled mesh flow-through electrodes and a single-component device structure. (d) Solution resistance as a function of angle between electrodes and buildup of bubbles on the electrodes in stagnant solution and in a flowing electrolyte with fluid velocity of 13.2 cm s<sup>-1</sup> during electrolysis at 2.5 V. (e) and (d) Reproduced with permission.<sup>162</sup> Copyright 2016, The Electrochemical Society. (e) Detailed schematic of a passive membrane-less electrolysis cell utilizing buoyancy-driven product separation. (f) The comparison of hydrogen cross-over percentage is presented for both symmetric and asymmetric electrodes under different angles, with operations conducted at a current density of 20 mA cm<sup>-2</sup>. Reproduced with permission.<sup>163</sup> Copyright 2023, The Royal Society of Chemistry. (g) Separation of gas products at an intermediate position and at the exit when the flow rate varies. Reproduced with permission.<sup>164</sup> Copyright 2021, American Chemical Society. (h) Design concept for capillary-fed electrolysis cell and its 30 days stability test. Reproduced with permission.<sup>165</sup> Copyright 2022, Springer Nature.



separation (Fig. 7(d)). Alternatively, Esposito *et al.*<sup>163</sup> implemented an asymmetric mesh electrode (Pt deposited onto only outer surfaces of Ti mesh) that leveraged buoyancy for gas separation (Fig. 7(e)), achieving a crossover rate of about 1%, though with subpar electrolytic efficiency (Fig. 7(f)). It operates stably for 75 minutes under continuous illumination with 0.5 M H<sub>2</sub>SO<sub>4</sub>, coupled with a floating photovoltaic module. Consequently, microfluidic membrane-less electrolysis cells have been developed to improve both gas crossover and high ohmic resistance issues and they have no need for pumps. De *et al.*<sup>164</sup> integrated bifunctional nickel nitride (Ni<sub>3</sub>N/Ni) catalysts into electrolysis cells (Fig. 7(g)), achieving 6-hours stable operation. However, at higher current densities, additional strategies are needed. Although this approach is still in its early stages, there is significant potential for enhancing its activity, stability, and electrolysis efficiency. However, the key issue is that its size is too small for industrial DSE with high currents. In addition, a new type of membrane-less electrolysis cells using pure water conditions has been designed. Hodges *et al.*<sup>165</sup> proposed a capillary-fed electrolysis (CFE) cell concept, enabling bubble-free operation for hydrogen and oxygen evolution electrodes. Their alkaline capillary feed electrolysis cells outperform commercial cells, achieving a voltage of only 1.51 V at 500 mA cm<sup>-2</sup> and 85 °C. It showed stable performance over a long period of time lasting from one day to 30 days at 80 °C (Fig. 7(h)) and room temperature and is considered by the authors of this paper to be of interest in future DSE.

## 4.2 Membrane-based electrolysis cells

**4.2.1 Alkaline water/anion exchange membrane electrolysis cells.** AWE is well developed, and its main components are cathode and anode electrodes, as well as diaphragm/membrane, which are easy to realize large-scale applications and have been widely used as a reactor for SWE. Diaphragm/membrane is possible to guarantee ion transfer while still minimizing gas crossover. However, AWE still suffers from some commonly recognized problems, including high energy consumption (e.g., more than 4 kW h N<sup>-1</sup> m<sup>-3</sup>), relatively low operating current density, slow temperature rise start-up time, and large equipment size.<sup>3,9</sup> The alkaline electrolyte also reacts with CO<sub>2</sub> in the air to form insoluble carbonates such as K<sub>2</sub>CO<sub>3</sub>, which hinder the transfer of gases and reactants.<sup>17</sup> AEMWE stands out for its ability to combine the advantages of both AWE and PEMWE. AEMWE can operate at high efficiency with lower costs, representing a promising direction for sustainable and green hydrogen production. At the same time, as mentioned above, the high pH condition minimizes the competitiveness of CER relative to OER, which makes AEMWE more attractive than PEMWE and of great interest to DSE.

In DSE, modifications to the electrode structure have been described in detail in Section 3.2. Next, we focus on the impact of operating modes and other key components on long-term stability. The typical mode of operation is to use a symmetrical feed of alkalized seawater, however, asymmetrical feeding may avoid the competitive CER at the anode. Strasser *et al.*<sup>166</sup> describe an electrolysis cell that circulates neutral seawater at

the cathode and pure KOH at the anode, demonstrating excellent corrosion resistance and OER selectivity. Starting at 1.7 V with a current density of 200 mA cm<sup>-2</sup>, the voltage rose by 8–10 mV every 12 hours, accumulating to about 100 mV over 100 hours (Fig. 8(a)). While the NiFe-LDH electrodes remained stable, the degradation was linked to the anode catalyst, collector, or membrane components. Although few studies have been done on the key components such as flow fields in DSE, there have also been some studies into structural designs to facilitate bubble removal in AMEWE using KOH or water.<sup>167</sup> Duan *et al.*<sup>168</sup> introduced a novel concave-convex mastoid polar plate that enhances gas-liquid distribution uniformity in the flow channel. Using a three-dimensional model for numerical simulations, they optimized the structure with a multi-objective genetic algorithm. The optimized design achieved an 8.40% improvement in electrolyte flow rate uniformity while maintaining a lower pressure drop compared to the original structure (Fig. 8(b)), which can be beneficial for the long-term stable operation.<sup>3</sup> In addition, Shi *et al.*<sup>169</sup> designed a pH asymmetric electrolysis cells (Fig. 8(c)) incorporating a Na<sup>+</sup> exchange membrane for direct seawater decomposition to prevent Cl<sup>-</sup> corrosion by blocking Cl<sup>-</sup> transport to the anode, and mitigated Mg<sup>2+</sup> and Ca<sup>2+</sup> precipitation in near-neutral seawater (pH < 9.5). The output cathode electrolyte is maintained at pH 8.5 at 100 mA cm<sup>-2</sup>, showing a stable voltage response. After 120 hours of water-splitting, only a slight voltage increase is needed to reach 100 mA cm<sup>-2</sup> after refreshing the solution, confirming the system's durability (Fig. 8(d)). Alternatives to the anode include electronic mediators or small organic molecules that can replace slow OERs, enabling reactions at low voltages to avoid OERs and potentially eliminate chlorine emissions,<sup>44,170</sup> which is not what the review is exploring.

**4.2.2 Proton exchange membrane electrolysis cells.** In fact, PEMWE is more suitable for large-scale freshwater electrolysis or DSE, which not only has the advantage of generating large current densities and high hydrogen purity for sustainable operation, but also can be coupled with intermittent renewable energy sources.<sup>4,174</sup> In SWE, we have already mentioned in Section 2.1 that under acidic conditions, CERs are severely competitive with OERs. In addition, cations in seawater have a higher affinity for sulfonic acid groups in Nafion membranes used in PEMWE compared to protons. This displacement of protons reduces proton transport and conductivity in the membrane, leading to increased ohmic losses and higher cell voltage. The affinity order for Nafion membranes is Ca<sup>2+</sup> > Mg<sup>2+</sup> > K<sup>+</sup> > Na<sup>+</sup> > H<sup>+</sup>.<sup>175</sup> These cations can migrate and form precipitates deposited on the cathode.<sup>176</sup> Therefore, it is difficult for PEMWE to maintain efficient and stable operation in seawater electrolysis. However, studies have been conducted to eliminate the presence of Cl<sup>-</sup> on the anode side of PEMWE in order to make it suitable for DSE. Skumari *et al.*<sup>171</sup> developed an operating mode for a PEMWE using humidified seawater vapor (80% relative humidity) at the anode and dry N<sub>2</sub> at the cathode. At a constant cell voltage of 1.6 V from solar photovoltaics, this system demonstrated greater stability compared to one using liquid seawater, but the cell voltage was lower than



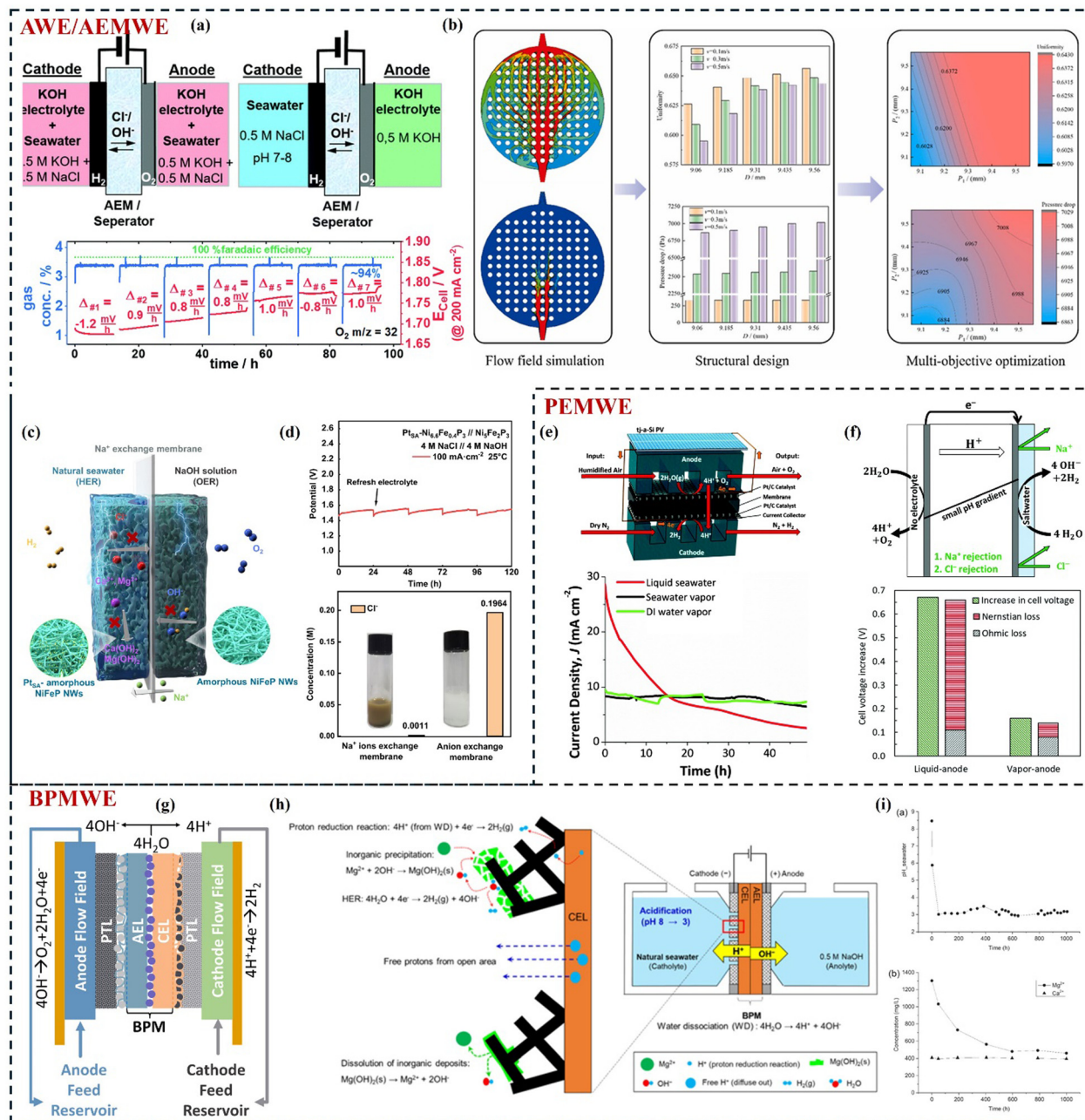


**Fig. 8** (a) Symmetric alkalinized 0.5 M NaCl feed and asymmetric 0.5 M NaCl feed at the cathode and 0.5 M KOH feed at the anode. Reproduced with permission.<sup>166</sup> Copyright 2020, The Royal Society of Chemistry. (b) Machine learning aids the optimization process of flow field in AWE.<sup>168</sup> Copyright 2024, Elsevier. (c) Asymmetric electrolysis cell with  $\text{Na}^+$  exchange membrane. (d) Long-term stability test of the asymmetric electrolysis cell with  $\text{Na}^+$  exchange membrane at  $100 \text{ mA cm}^{-2}$  and  $\text{Cl}^-$  concentration in anode electrolytes. (c) and (d) Reproduced with permission.<sup>169</sup> Copyright 2023, Springer Nature. (e) Schematic of an electrolysis cell with anode: seawater vapor (80% relative humidity) and cathode: dry  $\text{N}_2$  and current density versus time at an applied voltage of 1.6 V for different feedstock at the electrolysis tank anode. Reproduced with permission.<sup>171</sup> Copyright 2016, The Royal Society of Chemistry. (f) Schematic of an electrolysis cell using a vapor feed at the anode and saltwater at the cathode and the effect of  $\text{Na}^+$  in solution on the overpotential caused by pH gradients. Reproduced with permission.<sup>172</sup> Copyright 2021, The Royal Society of Chemistry. (g) Schematic of an electrolysis cell with BPM. Reproduced with permission.<sup>33</sup> Copyright 2023, Elsevier. (h) Mechanism of seawater acidification via synergistic effects between inorganic precipitation on the cathode surface and proton flux from BPM. (i) pH variation of bulk seawater during 1000 hours of BPMWE operation at  $20 \text{ mA cm}^{-2}$ , along with changes in concentrations of  $\text{Mg}^{2+}$  and  $\text{Ca}^{2+}$ . (h) and (i) Reproduced with permission.<sup>173</sup> Copyright 2023, The Electrochemical Society.

anticipated, indicating potential for further optimization (Fig. 8(e)). Rossi *et al.*<sup>172</sup> switched the anode seawater electrolyte to water vapor while feeding the cathode side with seawater. However, the membrane is still damaged due to the presence of

$\text{Na}^+$  in the cathode, which can lead to poor membrane stability (Fig. 8(f)).

**4.2.3 Bipolar membrane electrolysis cells.** Unlike conventional unipolar PEMWE or AEMWE systems, the working principle

involves water penetrating the BPM (Fig. 8(g)), where it ionizes into  $H^+$  and  $OH^-$  at the junction of the cation and anion exchange layers.  $H^+$  and  $OH^-$  are then transported to the anode and cathode through the cation exchange layer (CEL) and anion exchange layer (AEL), respectively.<sup>177</sup> Marin *et al.*<sup>33</sup> developed a bipolar membrane water electrolysis (BPMWE) cell specifically designed with asymmetric brine electrolyte conditions, enabling the efficient production of  $H_2$  and  $O_2$  at elevated current densities. The selective transport of cations within the CEL restricts  $Cl^-$  to the anode, while the AEL facilitates a localized alkaline pH at the anode. This configuration yields an exceptionally low transport rate of  $Cl^-$  and enhances the selectivity for the OER. Consequently, the faradaic efficiency (FE) for the oxidation of  $Cl^-$  to the corrosive hypochlorite at the anode is minimized to a mere 0.005%, significantly lower than the 10% FE observed in PEMWE systems. In addition,  $K^+$ <sup>178</sup> and  $SO_4^{2-}$ <sup>179</sup> permeation across the membrane is also inhibited, the main reason is that, for example,  $H^+$  flux inhibits  $K^+$  crossover to the cathode, which also highlights an interesting approach to mitigating contaminant ion crossover during the electrolysis process. Kim *et al.*<sup>179</sup> created a locally alkaline environment in the anode chamber with KOH solution and a locally acidic environment in the cathode chamber with  $H_2SO_4$  solution in BPMWE. This setup optimized pH conditions for each half-reaction, reducing anodic competition for CER and  $Ca^{2+}/Mg^{2+}$  precipitation at the cathode. Additionally, an optimized porous cathode with an open region and BPM facilitated proton generation through water dissociation (Fig. 8(h)).<sup>180</sup> The reduction of protons near the cation exchange layer, along with proton flow through the open region, minimized inorganic scaling and acidified the seawater, resulting in BPMWE stability for 1000 hours (Fig. 8(i)).<sup>173</sup> The advantages and challenges of various electrolysis cells (*e.g.* AWE, AEMWE, PEMWE, BPMWE) under seawater conditions are summarized in Table 2.

#### 4.2.4 Membrane degradation and strategies for improvement.

In view of the different cell configurations mentioned above, the stability of the membrane has a great impact on the long-term operation of the DSE. Therefore, we systematically analyzed the degradation mechanism of membranes in DSE,

focusing on AEMs due to their mature research in DSE. The degradation of membrane in DSE is mainly divided into basic and seawater effects. In terms of basic effects, ionomer and membrane have the same degradation pathways, which is relative to the ionomer and membrane structure. Fig. 9(a) illustrates various failure mechanisms of AEMs in detail, highlighting basic chemical degradation pathways, including nucleophilic substitution, elimination, phenyl oxidation, and methyl or proton rearrangements, all influenced by their polymer structure.<sup>28</sup> These degradation pathways compromise membrane integrity, leading to potential solubility of ionomer fragments and reduced ionic conductivity due to the loss of charged end groups.<sup>182</sup> Finally, the locally increased  $OH^-$  concentration exacerbated the degradation due to water transport limitations.<sup>183</sup> In terms of seawater effects, in addition to the chemical degradation caused by CER and the physical/mechanical degradation caused by bubbles and precipitation coverage mentioned in Sections 2.2 and 2.3, complex ions in seawater can also damage membranes and ionomers. There are ions with the same charge as the fixed membrane charge (co-ions) and ions with the opposite charge to the fixed membrane charge (counter-ions) in seawater. Counter-ions compete with  $OH^-$  transport in the AEM, increasing membrane resistivity and slowing water transport, thereby reducing membrane hydration.<sup>183</sup> The effects of complex ions in seawater on membranes are summarized in Table 3.

Improved electrode design strategies for degradation (bubble/precipitation coverage, CER corrosion, etc.) are also beneficial to the performance of the membrane in long-term operation, as described in detail in Section 3. In addition, some specific strategies have been proposed to address the above membrane degradation. Firstly, Kim *et al.*<sup>184</sup> developed high-molecular-weight hexyltrimethylammonium-tethered polycarbazoles (HQPC-TMA-x) membrane that exhibited high ionic conductivity, mechanical robustness, and alkaline stability. HQPC-TMA-x also helps mitigate ionomer adsorption issues on electrodes due to the polycarbazole backbone. It demonstrated outstanding performance in both pure water and direct seawater electrolysis. HQPC-TMA-2.4 also showed impressive durability, maintaining

Table 2 Comparison of AWE, AEMWE, PEMWE, and BPMWE in seawater condition

Type	Advantages	Challenges
AWE <sup>3,9</sup>	1. Mature, commercially available 2. Lower material costs 3. Robust design	1. Low efficiency and current density 2. Gas crossover 3. Slow response to variable conditions
AEMWE <sup>3,9,45</sup>	1. High efficiency and current density 2. Compact, modular design 3. High-purity hydrogen production 4. Lower material costs	1. Limited membrane durability 2. Low $OH^-$ conductivity 3. Precipitation blocking membrane and electrodes
PEMWE <sup>4,174,181</sup>	1. High efficiency and current density 2. Compact, modular design 3. High-purity hydrogen production	1. Expensive catalysts and components 2. More prone to CER 3. $Ca^{2+}/Mg^{2+}$ , etc. displace $H^+$ in membrane <sup>175</sup>
BPMWE <sup>177,179</sup>	1. Separate anode/cathode environments 2. Flexible anode/cathode pH control 3. Reduce $Cl_2$ and precipitation	1. Less mature 2. Complex membrane fabrication



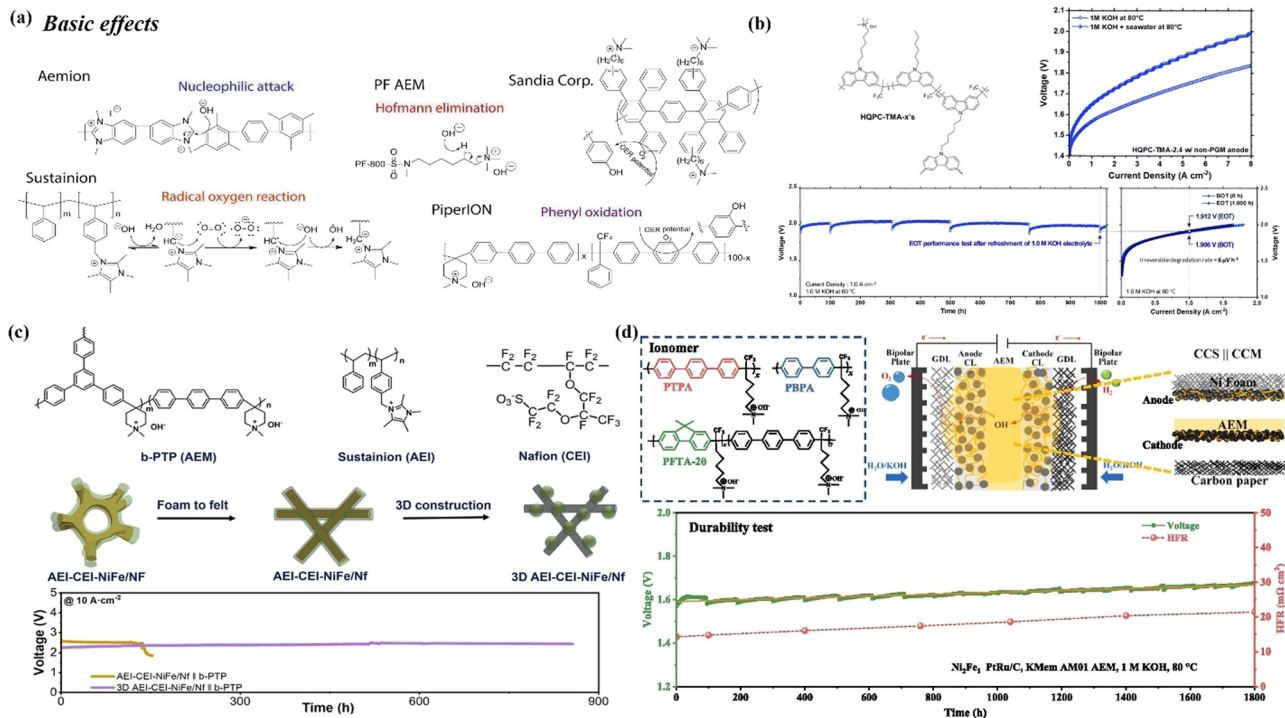


Fig. 9 (a) Examples of some typical degradation pathways of membrane materials. Reproduced with permission.<sup>28</sup> Copyright 2020, Elsevier. (b) The schematic structure of high-molecular-weight hexyltrimethylammonium-tethered polycarbazoles (HQPC-TMAs) is presented, along with the electrolysis performance of HQPC-TMA-2.4 in 1.0 M KOH and 1.0 M KOH + seawater. Additionally, a 1000-hour durability test of the 1.0 M KOH electrolyzer, operated at 1.0 A cm<sup>-2</sup> and 60 °C.<sup>184</sup> Copyright 2024, The Royal Society of Chemistry. (c) Molecular structures of AEM: branched poly(terphenyl piperidinium) (b-PTP), AEI: Sustainion XB-7, and CEI: Nafion, along with a schematic representation of the various catalyst-PTL interfaces and stability tests at 10 A cm<sup>-2</sup> (Pt/C as the cathode). The operational conditions included a cell temperature of 80 °C and 1 M KOH as the electrolyte). Reproduced with permission.<sup>185</sup> Copyright 2024, Wiley. (d) Chemical structures of ionomers (PTPA, PBPA, and PFTA-20) and an illustration of CCS || CCM MEA configuration is presented. Additionally, a long-term durability test of AEMWE was conducted at a constant current density of 1.0 A cm<sup>-2</sup> at 80 °C. Reproduced with permission.<sup>186</sup> Copyright 2025, Elsevier.

Table 3 Impact of seawater ions and impurities on membrane performance<sup>12</sup>

Ion	Concentration (mol kg <sup>-1</sup> (H <sub>2</sub> O))	Effect
Cl <sup>-</sup>	0.56576	CER (corrosion), <sup>45</sup> reducing the conductivity <sup>166</sup>
Na <sup>+</sup>	0.48616	No significant adverse effects reported
Mg <sup>2+</sup>	0.05475	Precipitate covering the membrane <sup>28</sup>
SO <sub>4</sub> <sup>2-</sup>	0.02927	Affecting the OH <sup>-</sup> transport and reducing the conductivity <sup>45</sup>
Ca <sup>2+</sup>	0.01065	Precipitate covering the membrane <sup>28</sup>
K <sup>+</sup>	0.01058	No significant adverse effects reported
HCO <sub>3</sub> <sup>-</sup>	0.00183	Concentration polarization, <sup>183</sup> reducing the conductivity <sup>187</sup>
Br <sup>-</sup>	0.00087	Corrosion and poison <sup>29</sup>
CO <sub>3</sub> <sup>2-</sup>	0.00027	Concentration polarization, <sup>183</sup> reducing the conductivity <sup>187</sup>
F <sup>-</sup>	0.00007	Corrosion and poison <sup>29</sup>
Biofouling	NA	Poison and covering membrane <sup>188</sup>
OH <sup>-</sup>	0.00001	No adverse effects reported

a high current density of 1.0 A cm<sup>-2</sup> for 1000 hours, with minimal irreversible degradation rates of 52 and 6  $\mu$ V h<sup>-1</sup> for platinum group metal (PGM)-free cells, respectively (Fig. 9(b)). In addition, from the point of view of enhanced membrane conductivity (strong OH<sup>-</sup> transport) and strong adhesion of the ionomer, Zheng *et al.*<sup>185</sup> used a branched poly(terphenyl piperidinium) (b-PTP) AEM<sup>189</sup> that proved to be robust, and a blended ionomer combining strong adhesive Nafion ionomer and strong OH<sup>-</sup> transport capacity of the Sustainion ionomer, which

allowed the AEMWE to operate for more than 800 hours at 10 A cm<sup>-2</sup> (Fig. 9(c)). Li *et al.*<sup>186</sup> designed an anion exchange ionomer (AEI) featuring a non-rotatable fluorenyl backbone that minimizes phenyl adsorption and enhances oxidation stability, resulting in 1800 h with a low voltage of 1.6 V at 1.0 A cm<sup>-2</sup>. Notably, they proposed a hybrid MEA design, combining a coated-catalyst substrate anode and a coated-catalyst membrane cathode, addressing membrane swelling and enhancing MEA stability through strong bonding between the anode catalyst

layer and the porous substrate (Fig. 9(d)). Although the above studies did not directly conduct long-term stability tests under seawater electrolysis conditions, they still provide guidance for the design of durable membranes and ionomers for DSE.

#### 4.3 Solid oxide-based electrolysis cells

In addition to the above-mentioned electrolysis cells operating at low temperatures, high-temperature solid oxide electrolysis cells (SOECs) using seawater operating at thermally driven high temperatures (800–1000 °C) have also been reported. In a high-temperature SOEC, steam is evaporated from the water and transported to the cathode to produce H<sub>2</sub>, and the resulting O<sub>2</sub> passes through the solid oxide membrane to the anode to form O<sub>2</sub>.<sup>190</sup> Operating at thermally driven high temperatures results in lower costs relative to electrical energy. In addition, high operating temperatures increase reaction kinetics and improve overall electrolysis efficiency. Theoretically, the energy conversion efficiency of a SOEC can exceed 100% if the absorbed heat is considered to be free of charge. The absence of any impurities in the water vapor also greatly benefits the lifetime of the membrane and catalyst. However, seawater electrolysis in SOEC can be problematic, including the long-term durability requirements of the electrodes and damage to the electrolysis cells from trace impurities in seawater vapor.<sup>191</sup> Liu *et al.*<sup>192</sup> used SOEC to split untreated seawater, achieving a hydrogen production rate of 183 mL min<sup>-1</sup> and a degradation rate of 4.0% over 420 hours at a constant current density of 200 mA cm<sup>-2</sup>. The energy conversion efficiency was 72.47%, without reusing high-temperature exhaust gas. However, they also found that ppm salts were still present in the vapor and that the tubes or cells could clog at certain points after 420 hours of operation. Not only that, high temperatures may require catalysts with excellent thermal stability,<sup>193</sup> for example, Hauch *et al.*<sup>194</sup> reported that continuous steam electrolysis at high current densities (1000 mA cm<sup>-2</sup>) caused significant microstructural degradation at the oxygen electrode-electrolyte interface and a marked increase in ohmic resistance. Most of the catalyst engineering strategies proposed in the current reviews have focused on low-temperature water electrolysis, with little involvement in high-temperature water electrolysis. Whether all strategies can be applied to high-temperature water electrolysis is not clear, and thus they are still in the early stages of development.

#### 4.4 Electrolysis cell integration and scaling-up

Integrating different technologies into a single system offers the potential to improve efficiency, reduce costs, and address complex challenges more effectively. Nocera *et al.*<sup>195,196</sup> recently developed the forward osmosis water electrolysis (FOWS) cells, streamlining seawater electrolysis by combining reverse osmosis desalination with freshwater electrolysis. This system utilizes brine directly, mitigating issues with impurities and energy losses. The FOWS consists of a single electrochemical chamber separated from seawater by a semi-permeable membrane, with a 0.8 M NaPi buffer solution on one side and 0.6 M NaCl on the other. The use of cellulose acetate membranes to filter out anions and cations such as Ca<sup>2+</sup>, Mg<sup>2+</sup>, CO<sub>3</sub><sup>2-</sup> and Cl<sup>-</sup> from seawater from the hydrolysis region

(Fig. 10(a)). Continuous operation requires balancing freshwater consumption and introduction by adjusting the concentration gradient and electrolysis current density (Fig. 10(b)). With 0.8 M NaPi and a platinum catalyst, the system maintained a stable electrolysis at 250 mA cm<sup>-2</sup> for 48 hours (Fig. 10(c)), achieving nearly 100% Faraday efficiency. However, challenges like gas crossover due to the lack of a barrier between hydrogen and oxygen, and Cl<sup>-</sup> diffusion from seawater remain. Logan *et al.*<sup>197</sup> suggested using an osmosis assembly between electrodes to separate gases (Fig. 10(d)), but Cl<sup>-</sup> diffusion and HER catalyst selectivity and stability issues in seawater need further addressing.

Based on the above research about the integration of *in situ* seawater purification technologies and water electrolysis technologies, Xie *et al.*<sup>34</sup> developed an innovative DSE system for hydrogen production, operating at 250 mA cm<sup>-2</sup> for over 3200 hours. This system integrates an *in situ* water purification mechanism that uses a self-driven phase transition process and seawater electrolysis. It features a hydrophobic, porous polytetrafluoroethylene (PTFE) membrane as a gas pathway, alongside a concentrated KOH solution acting as a self-dampening electrolyte (Fig. 10(e)). The difference in vapor pressure between seawater and the KOH allows for the evaporation of seawater, which then diffuses through the membrane and is re-liquefied, effectively filtering out contaminants like Cl<sup>-</sup>, Mg<sup>2+</sup>, and SO<sub>4</sub><sup>2-</sup>. This results in a continuous supply of pure water for hydrogen production from seawater. Due to the efficient isolation of impurities in the electrolysis cells, the integrated cell stack utilizes commercial MoNi/Ni foam for the anode and PtNi mesh for the cathode (Fig. 10(f)). Additionally, in collaboration with China Dongfang Electric Corporation, the team developed the “Dongfu-1,” the first offshore wind-driven hydrogen production platform without desalination.<sup>39</sup> During sea trials in May 2023, it produced 1.3 N m<sup>3</sup> h<sup>-1</sup> of hydrogen, exceeding the target energy consumption of 5 kW h N m<sup>-3</sup>, and operated for over 240 hours with over 99.99% ionic barrier efficiency against seawater impurities (Fig. 10(g)) and there is no change in water migration in PTFE membranes (Fig. 10(h)), ensuring hydrogen purity levels of 99.9% to 99.99%.

For large-scale DSE, there is still a trade-off between economic factors and performance stability for different electrode materials during the transition from laboratory scale to industrial scale. Specifically, commercial Pt-based electrocatalysts can only operate in natural seawater for less than 1 hour due to toxic substances,<sup>198</sup> while commercial RANEY® Ni suffers severe Cl<sup>-</sup> corrosion.<sup>199</sup> Commercial IrO<sub>2</sub><sup>200</sup> and RuO<sub>2</sub><sup>201</sup> also face selectivity and durability challenges. Therefore, directly applying existing commercial catalysts to DSE for large-scale applications is impractical. Most ampere-level DSE electrodes currently employ self-supported electrodes developed on metal foam substrates. Metal foams act not only as conductors and carriers but also enable their own metal ions to replace metal salt precursors, directly participating in electrocatalyst assembly. This facilitates the growth of diverse nanostructures (e.g., nanowires, nanosheets, nanoarrays), effectively enhancing catalytic activity while reducing costs and stability uncertainties



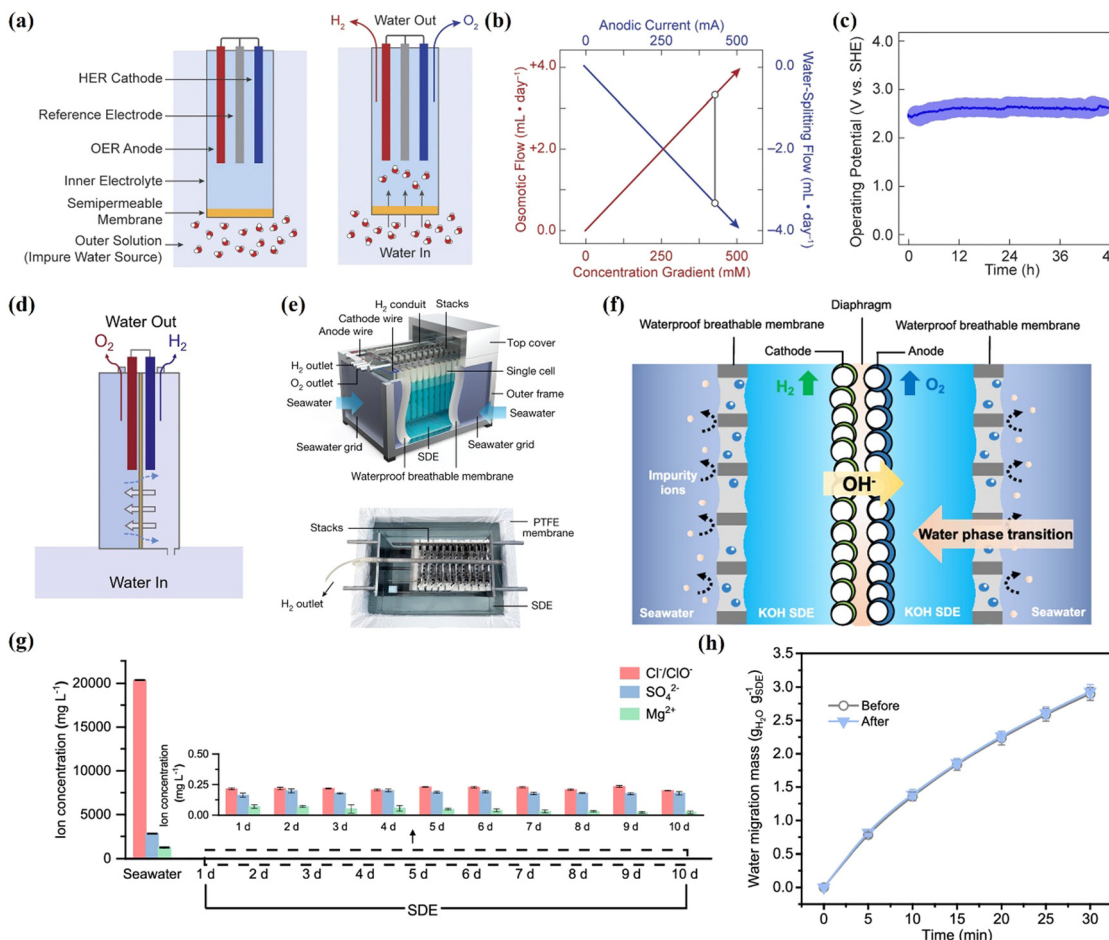


**Fig. 10** (a) Key components of the FOWS cell for use in contaminated water sources and their operation process. (b) The rates of water influx (red) and outflux (blue). (c) Stability test at 250 mA with a 0.8 M NaPi inner electrolyte solution and 0.6 M NaCl outer electrolyte solution. (a)–(c) Reproduced with permission.<sup>196</sup> Copyright 2020, National Academy of Sciences. (d) The membrane divides the electrodes into two chambers, with desalinated water collected from the catholyte. Reproduced with permission.<sup>197</sup> Copyright 2021, Elsevier. (e) Actual picture of the integrated stack of the AWE with porous PTFE membrane. Reproduced with permission.<sup>34</sup> Copyright 2022, Springer Nature. (f) Electrolysis of seawater using a water phase-transition migration mechanism through porous PTFE membrane. (g) The average ion concentrations in the innovative DSE cell and Xinghua Bay seawater. (h) Water migration behavior of the porous PTFE membrane before and after 10 days of use. Reproduced with permission.<sup>39</sup> Copyright 2024, Springer Nature.

associated with ionomer binders.<sup>202</sup> Taking nickel foam (NF) as an example, although its intrinsic DSE catalytic activity is modest ( $\eta = 573$  at  $10 \text{ mA cm}^{-2}$ ),<sup>203</sup> its catalytic performance and durability can be dramatically improved through catalyst loading and modification (see Table 1). Combined with low cost, NF emerges as a strong candidate for DSE electrodes. Additionally, metal meshes/felts offer the advantages of lower cost, higher mechanical strength, and superior chemical stability.<sup>204</sup> Relative studies have explored stainless steel mesh (SSM) substrates as electrodes for various electrochemical reactions. For example, Lyu *et al.*<sup>205</sup> investigated commercial 316 SS and 304 SS as OER electrodes in natural seawater electrolysis. They found that 304 SS exhibited inferior corrosion resistance compared to 316 SS in neutral and mildly alkaline seawater electrolytes due to direct metal dissolution and CER. Increasing Mo content in 304/316 SS can enhance their stability and performance in seawater electrolysis. Notably, SSM has demonstrated performance surpassing commercial  $\text{RuO}_2$  and

$\text{IrO}_2$ .<sup>202</sup> These cost-effective, durable substrates also enable the development of 3D electrodes with controlled microstructures, enhancing local mass transfer to accommodate industrial-level high current densities while maintaining catalytic activity. We strongly recommend utilizing these advantageous catalytic substrates in DSE electrode R&D to further improve performance, selectivity, and long-term durability.

Compared to catalyst design, DSE device engineering presents greater challenges. Integrated DSE systems require balancing catalyst cost with prolonged durability. While academia has extensively studied seawater electrolysis catalysts and proposed numerous strategies to address harsh operating conditions, two critical gaps remain: (1) most studies overlook practical challenges of real seawater in application scenarios; (2) practical implementation demands innovative catalyst engineering and optimization of catalyst layer characteristics (uniformity, thickness) alongside other components like porous transport layers (PTL material properties, hydrophilicity, thickness). Furthermore, catalyst synthesis

methods profoundly impact scalable production, essentially requiring a paradigm shift from materials chemistry to chemical engineering. Despite catalysis being a well-established field, knowledge about catalyst mass production remains scarce, though it ultimately determines process feasibility. Industrially, catalyst mass-production formulas remain closely guarded secrets, still dominated by empirical approaches. Taking widely studied NiFe-LDH in DSE as an example, electrochemical deposition and *in situ* growth (*e.g.*, hydrothermal methods) offer simple and scalable fabrication. However, these methods suffer from time/energy intensiveness, typically requiring hours (even the fastest electrodeposition takes 3–15 min<sup>206</sup>). Notably, Tian *et al.* developed an ultrafast method by immersing Prussian blue analogs (PBA) chemically deposited on NF into 1 M KOH solution, achieving NiFe-LDH nanoparticle immobilization on NF within 10–90 s without post-treatment. The NiFe-LDH-20s/NF electrode demonstrates exceptional activity with low overpotential ( $\sim 0.240$  V at 10 mA cm $^{-2}$ ), small Tafel slope (38 mV dec $^{-1}$ ), and stable performance during 15-h multi-step chronopotentiometric testing

(50–500 mA cm $^{-2}$ ).<sup>207</sup> With advancing catalytic technologies, academia urgently needs to deepen understanding of catalyst scale-up to comprehensively bridge synthesis–mechanism–process relationships. This requires interdisciplinary expertise spanning chemistry (synthesis, physics, analysis), materials science, and chemical/mechanical engineering (reactor design). We therefore advocate for cross-disciplinary collaborative development in the transition of DSE technologies from laboratory to industrial scale. A comparison table of key performance indicators for different types of electrolysis cells (AWE, PEM, AEMWE and BPMWE) is given for reference (Table 4).

## 5 System-level integration and considerations for long-term stability

The coupling of renewable energy sources such as wind turbines with electrolysis cells is an important system integration for future DSE technology for green hydrogen production.

Table 4 Comparison of key performance indicators of different electrolyzer types in DSE

Anode	Cathode	Electrolyte	T (°C)	Performance	Ref.
<b>AWE</b>					
MHCM-z-BCC	NiMoS	Neutral phosphate-buffered seawater	25	2.1 V@10 mA cm $^{-2}$ , current density dropped to 100% after 10 h	208
NiNS	NiNS	Neutral phosphate-buffered seawater	25	1.8 V@48.3 mA cm $^{-2}$	209
Co–Fe <sub>2</sub> P	Co–Fe <sub>2</sub> P	0.5 M NaCl + 1.0 M KOH	25	1.69 V@100 mA cm $^{-2}$ , 22 h@100 mA cm $^{-2}$	210
SSM	Ni–MoN	1 M KOH + seawater	25	1.783 V@500 mA cm $^{-2}$ , 100 h@500 mA cm $^{-2}$	211
NCMS/NiO	NCMS/NiO	5 M KOH + seawater	80	1.98 V@1000 mA cm $^{-2}$ , 30 d@100 mA cm $^{-2}$	212
S-(Ni,Fe)OOH	NiMoN	1 M KOH + seawater	25	1.837 V@500 mA cm $^{-2}$ , 100 h@500 mA cm $^{-2}$	101
Mo–Ni <sub>3</sub> S <sub>2</sub> /NF	PtNi mesh	30 wt% KOH (inner) + seawater (outer)	25	3200 h@250 mA cm $^{-2}$	34
NiFeP@Ag	Cu <sub>2</sub> S@Ni	1 M KOH + seawater	25	1.95 V@400 mA cm $^{-2}$ , 1200 h@400 mA cm $^{-2}$	213
<b>PEMWE</b>					
FeO <sub>x</sub>	FeO <sub>x</sub>	0.6 M NaCl + 0.1 M KOH	25	30 min	214
Ir black	Pt/C	Anode: water vapor Cathode: 0.5 M NaCl	80	2.37 V@500 mA cm $^{-2}$ , 1.5 h@500 mA cm $^{-2}$	172
(NiFe)C <sub>2</sub> O <sub>4</sub> /NF	Pt/C	1 M KOH + seawater	25	2.4 V@500 mA cm $^{-2}$ , 150 h@500 mA cm $^{-2}$	94
CoO <sub>x</sub> –Cr <sub>2</sub> O <sub>3</sub>	CoO <sub>x</sub> –Cr <sub>2</sub> O <sub>3</sub>	Seawater	60	1.87 V@1000 mA cm $^{-2}$ , 100 h@500 mA cm $^{-2}$	11
<b>AEMWE</b>					
Pt/C	Co <sub>3–x</sub> Pd <sub>x</sub> O <sub>4</sub> on MnO <sub>2</sub> -NF	Anode: 0.5 M NaCl + 1.0 M PBS Cathode: humidified N <sub>2</sub>	25	65 h@100 mA cm $^{-2}$	105
Pb <sub>2</sub> Ru <sub>2</sub> O <sub>7–x</sub>	Pt/C	0.6 M NaCl + 0.1 M NaOH	25	1.8 V@275 mA cm $^{-2}$ , 5 h@200 mA cm $^{-2}$	140
Fe, P–NiSe <sub>2</sub> NFs	Fe, P–NiSe <sub>2</sub> NFs	Anode: N <sub>2</sub> Cathode: seawater	25	1.7 V@305 mA cm $^{-2}$ , 1.8 V@200 h	215
NiFe-LDH	Pt/C	Anode: 0.5 M NaCl Cathode: 0.5 M KOH	25	12 h@1.7 V	166
RuMoNi	RuMoNi	1 M KOH + seawater	80	1.72 V@1000 mA cm $^{-2}$ , 240 h@500 mA cm $^{-2}$	87
Ni–FeOOH	Pt/C	1 M KOH + seawater	25	1.7 V@469 mA cm $^{-2}$ , 15 h@500 mA cm $^{-2}$	99
NiFe-LDH/Ni@Ni <sub>x</sub> S <sub>y</sub>	CoP/C/Ni@Ni <sub>x</sub> P <sub>y</sub>	1 M KOH + seawater	60	2 V@1000 mA cm $^{-2}$ , 100 h	152
<b>BPMWE</b>					
Ir@Ti fiber	Pt@Ti fiber	Anode: 0.5 M KOH Cathode: seawater	25	1000 h@100 mA cm $^{-2}$	173
Pt@Ti mesh	Pt@Ti mesh	Anode: 0.1 M NaOH Cathode: sea salt solution	—	Cell voltage was changed from –3.0 to –3.5 V (100 h@10 mA cm $^{-2}$ )	216
IrO <sub>x</sub> nanoparticles	Pt black	Seawater for both electrolytes	RT	Cell voltage increased by 0.90 V (>6 h operation; 250 mA cm $^{-2}$ )	33
Porous Pt	Porous Pt	Anode: 0.5 M NaOH Cathode: seawater	25	Cell voltage was stable at –2.3 V (100 h; 20 mA cm $^{-2}$ )	158



Specifically, the system-level integration is mainly composed of electrolysis cells and some auxiliary machines such as wind power generation system, seawater pumps, pipes, gas–water separation, hydrogen purification and storage systems.<sup>40</sup> In offshore wind power generation, wind turbines initially produce direct current (DC) energy, which is necessary for the electrolysis cells. However, a transformer is required to convert this to the appropriate voltage level. Pumps are used to supply seawater to the electrolysis cells continuously. Then, electrolysis cells produce hydrogen and oxygen at the cathode and anode respectively. To purify hydrogen and oxygen, it is essential to incorporate a cooling system and a drying phase to manage issues linked to water vaporization and the potential transfer of water across the membrane. The separation of the generated gases from the electrolyte is facilitated by a gravity-operated separator drum, which is typically installed at the top of the electrolysis cells. Actually, the lifespan of these auxiliary equipment is also a key factor in the long-term and stable operation of the entire DSE. For the corrosion of some ions in seawater such as  $\text{Cl}^-$  and biofouling, inlet and outlet pipes and other auxiliary machines require corrosion-resistant treatment to avoid leaks that could lead to unstable operation of the system, such as using corrosion-resistant materials (titanium alloys, nickel-based coatings, polymer-lined pipework, *etc.*)<sup>217–219</sup> or applying anti-fouling coatings. In addition, local chlorine generation has been shown to delay biofouling.<sup>220</sup> Maritime workers employ technologies such as cold spray<sup>221</sup> and plasma spray<sup>222</sup> to apply specialized coatings—like copper-doped polymers, metals, and silver-doped antifouling solutions—onto marine engineering equipment.<sup>223</sup> These targeted antifouling strategies aim to enhance their lifespan while minimizing environmental impact. Although copper and silver are effective for their antibacterial and antifouling properties, their potential ecological risks necessitate stringent regulation and ongoing improvements.<sup>224</sup> Here, we present typical effective antifouling references for consideration (Fig. 11(a) and (b)).<sup>225,226</sup> For the byproducts, such as precipitates (*e.g.*,  $\text{Mg}(\text{OH})_2$ ,  $\text{Ca}(\text{OH})_2$ ),<sup>227,228</sup> hypochlorite or hypochlorous acid,<sup>229,230</sup> *etc.* Some effective practical engineering guidance for the treatment of byproducts is provided. For example, sodium hypochlorite ( $\text{NaOCl}$ )<sup>231</sup> is formed by mixing chlorine gas from the anode with  $\text{NaOH}$  from the cathode in seawater electrolysis, and the resulting concentration of sodium hypochlorite is similar to that found in household and industrial bleach.<sup>232</sup> In addition, Badjatya *et al.*<sup>228</sup> adopted seawater electrolysis to produce  $\text{Mg}(\text{OH})_2$  as a precursor for Mg-based cement. After converting  $\text{Mg}(\text{OH})_2$  into  $\text{MgCO}_3$  by reacting with  $\text{CO}_2$  in a low-temperature carbonation curing step, the resulting Mg-based cement can exhibit compressive strength comparable to that achieved by Portland cement after only 2 days of curing. Furthermore, compressors may be required to store the produced hydrogen at pressures ranging from 1 to 30 bar. For safe storage, the generated hydrogen can also be contained in metal hydride tanks. Depending on the targeted purity level, additional drying of hydrogen can be carried out through cooling, dehydrogenation, and variable pressure adsorption to remove any residual water before it

is stored or introduced into the required distribution network. The location of the electrolysis cells in relation to the offshore wind farm not only affects the installation, but also the long-term stability of the whole system and ultimately its operating costs. Three different configurations<sup>233</sup> for electrolysis cells deployment have been considered (Fig. 11(c)):

(a) Onshore:<sup>35</sup> in this scenario, electricity generated offshore is transmitted through undersea cables to offshore substations, where the voltage is increased. The electricity is then further conveyed *via* high-voltage cables to an onshore electrolysis cell for large-scale hydrogen production. While this configuration may facilitate the construction and upkeep of electrolysis cells, it could lead to greater energy losses due to the lengthy transmission distances and the challenges associated with managing high-voltage power offshore. In addition to maintaining plant components and systems, ensuring the stable operation of electrolysis cells is a significant challenge. Renewable energy sources, like wind and solar, experience variability due to seasonal changes in wind patterns and solar intensity. This fluctuation in power input can lead to frequent starts and stops of the entire system, potentially causing harm to the electrodes of the electrolysis cells and diminishing their longevity.<sup>234</sup> Therefore, there is an analysis indicating that a single 7 MW cell stack undergoes 87 cycles per day. However, by utilizing three 2.33 MW cell stacks, this cycling can be notably reduced to just 35 cycles per day. This reduction could potentially enhance the longevity of the electrolysis cells, as frequent cycling contributes to the degradation of cell performance. On the downside, using multiple stacks may lead to higher capital costs, although the cost per kW for electrolysis cell stacks tends to decrease as their power capacity increases.<sup>235</sup>

(b) Offshore:<sup>236</sup> in this arrangement, electricity produced by offshore wind turbines is sent to a proximate offshore electrolysis cell. This system converts electricity into pressurized hydrogen, which is subsequently transported to the mainland through pipelines. This approach minimizes energy losses and may reduce the costs associated with long-distance electrical transmission. However, oxygen and hydrogen bubble dynamics, as well as the performance of liquid–gas separators, can be affected by the orientation of the equipment due to the motion of the offshore platform. Be aware that bubbles can cause physical/mechanical degradation in the electrolysis cells, Liu *et al.*<sup>39</sup> have proposed an innovative floating electrolysis system that harnesses wind and wave energy for direct electrolysis using dynamic seawater. The heart of this system is an electrolysis module developed by the Xie's group, which leverages the principle of aqueous phase transfer and integrates various modules, including energy storage, current conversion, hydrogen detection, and transport, for enhanced synergy. The electrolysis cell is designed to float within a seawater tank, addressing seawater fluctuations to improve system stability. To ensure the platform remains stable against displacement from cables or adverse weather conditions, it features counterweight modules and four anchoring points. Additionally, seawater tanks connected to the ocean *via* controlled valves help mitigate wave impact while facilitating direct interaction with



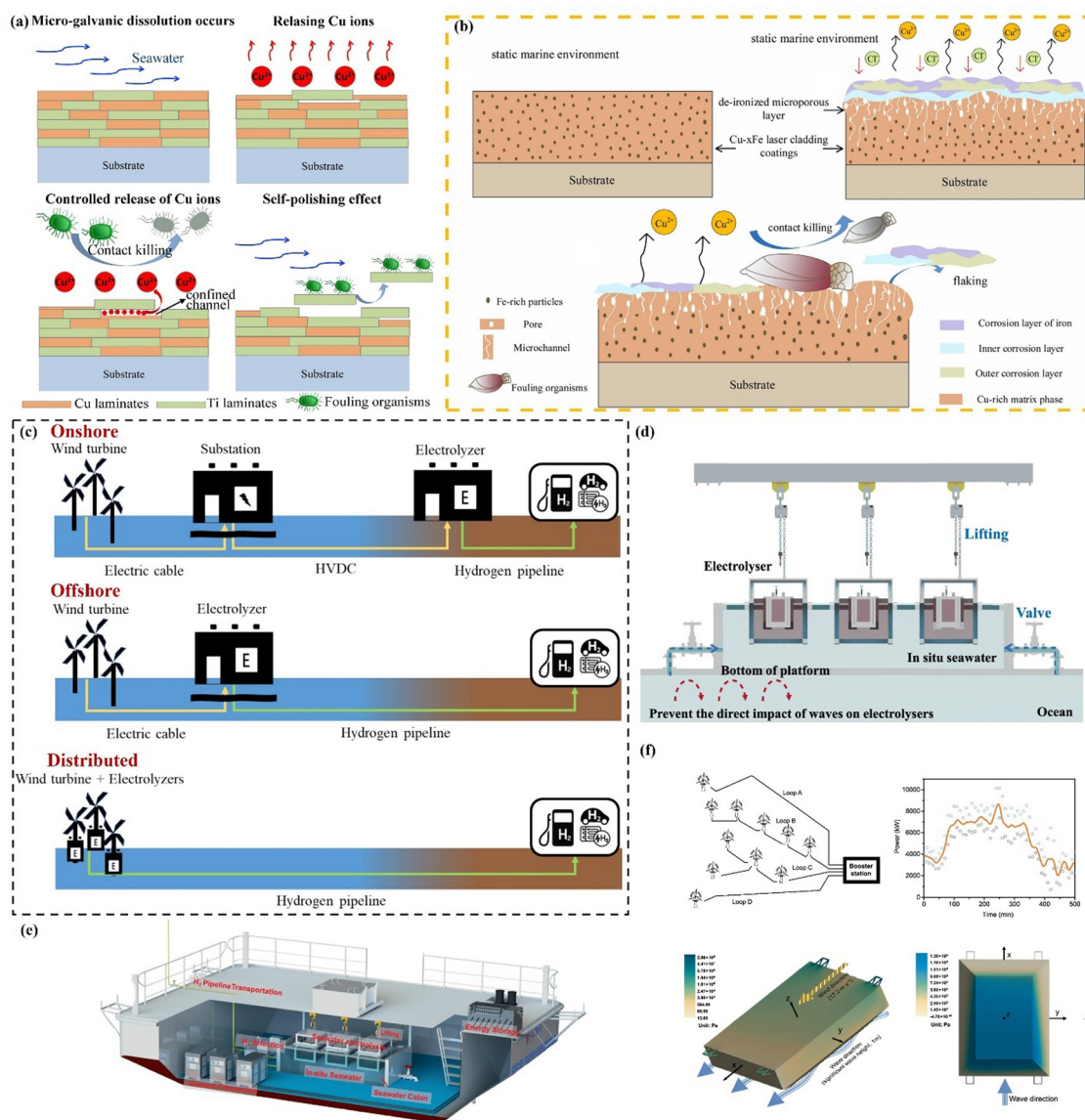


**Fig. 11** (a) Illustration of the antifouling mechanism for Cu-Ti composite and corrosion processes in Cu-Fe laser-clad coatings. Reproduced with permission.<sup>225</sup> Copyright 2021, Elsevier. (b) Schematic representation of corrosion processes in Cu-Fe laser-clad coatings. Reproduced with permission.<sup>226</sup> Copyright 2023, Elsevier. (c) Integrated electrolysis system configurations: onshore, offshore, and distributed. Reproduced with permission.<sup>233</sup> Copyright 2024, Elsevier. (d) Illustration of the seawater chamber connected to the ocean. (e) Illustration of the overall system consisting of power supply, electrolysis module, and auxiliary module. (f) The diagram shows the wind turbine network, fluctuation in turbine power with wind speed, and pressure and stress distribution of the floating platform in a fluctuating environment. (d)–(f) Reproduced with permission.<sup>39</sup> Copyright 2024, Springer Nature.

the electrolysis cells. Weighing about 48.5 tons, the platform is engineered to withstand wave forces. A sealed connection between the seawater tank and the electrolysis cells prevents sloshing and overflowing into the floating structure. The collaborative functionality of the offshore wind energy storage module, hydrogen detection module, and other auxiliary components ensures reliable and efficient operation of the system.

(c) Distributed:<sup>237</sup> this configuration entails the installation of small-scale electrolysis cells directly on each wind turbine, enabling immediate conversion of electricity into hydrogen at the generation site. The produced hydrogen is then compressed

and conveyed to the mainland. Individual (hydrogen) produced by each unit is transported through risers and can be collected in subsea manifolds for output. By localizing production, this setup decreases transmission energy losses and enhances the overall efficiency of hydrogen generation. The primary benefit of this configuration is that if one electrolysis cell malfunctions, the remaining wind turbines can still effectively generate hydrogen.<sup>238</sup> Relative strategies are employed to enhance the stability of systems like floating offshore wind (FOW) platforms (Fig. 11(d) and 11(e)). These strategies must account for adequate space for the electrolysis cell system and ensure robust

mechanical stability to maintain safety and performance once the electrolysis facility is integrated into the foundation (Fig. 11(f)).<sup>239</sup>

For the three configurations mentioned above, in the case of centralized onshore electrolysis, energy is transmitted to shore *via* a submarine high-voltage direct current (HVDC) cable. This approach is practical for nearby offshore locations, but it faces challenges such as energy losses and limited flexibility for future expansion. Conversely, both decentralized and centralized offshore systems utilize submarine hydrogen pipelines for energy transfer, which offer advantages over high-voltage cables. Hydrogen pipelines provide greater capacity for expansion and are generally more economical, as they are not constrained by the transmission limits of a single cable. Decentralized offshore systems are particularly advantageous due to their modular nature, allowing for continuous hydrogen production even if one electrolysis cell or turbine fails. However, they face challenges related to operational complexity and maintenance, necessitating further validation in offshore conditions.<sup>238</sup> On the other hand, centralized offshore systems can compete effectively, particularly in terms of simplified maintenance for individual turbines. While centralized systems are generally less complex, a significant drawback is that hydrogen production ceases if a failure occurs in the system. Furthermore, economic analyses<sup>240</sup> reveal that distributed hydrogen production is the most cost-effective option, with a leveled cost of hydrogen (LCoH<sub>2</sub>) at \$13.34 per kg, followed closely by centralized production at \$13.66 per kg, and land-based production at \$14.10 per kg. Rogeau *et al.*<sup>241</sup> also indicate that offshore electrolysis is significantly cheaper in terms of LCoH<sub>2</sub>, particularly in deep-water scenarios (over 100 m), where the decentralized option is expected to gain favor over centralized systems in the coming years. However, these findings require further investigation and discussion to be fully validated while considering long-term stability and economy of system.

Finally, we analyzed and projected the future of three prominent seawater hydrogen production demonstration projects in China. The 100 kW-level seawater electrolysis system (20 N m<sup>3</sup> h<sup>-1</sup>) developed by the Dalian Institute of Chemical Physics (DICP) achieves a cell voltage of 1.59 V and DC power consumption of 3.80 kW h N<sup>-1</sup> m<sup>-3</sup> h<sup>-1</sup> H<sub>2</sub><sup>-1</sup> at a current density of 3000 A m<sup>-2</sup> through high-performance electrodes and wide-power-adaptation processes. The hydrogen purity exceeds 99.999%, with successful adaptation to offshore wind power fluctuations.<sup>242</sup> Xie Heping's team pioneered the phase transition migration-driven *in situ* direct seawater electrolysis technology. Utilizing PTFE membrane gas-liquid isolation and vapor pressure differential mechanisms, this desalination-free hydrogen production method was validated by a 10 N m<sup>3</sup> h<sup>-1</sup> prototype operating continuously for 240 hours in Xinghua Bay, Fujian. A 1.2 N m<sup>3</sup> h<sup>-1</sup> floating platform for seawater hydrogen production *via* renewable energy achieved the first direct integration with offshore wind power under challenging conditions (wind scale 3–8, wave height 0.3–0.9 m) in Xinghua Bay, maintaining stable operation for 10 days.<sup>243</sup> The “Integrated

Offshore Green Hydrogen-Methanol-Ammonia Production System” jointly developed by National Energy Group Hydrogen Technology Co., Ltd, Yantai CIMC Raffles Offshore Engineering Co., Ltd, and others has received China Classification Society (CCS) certification. Combining off-grid PEM/alkaline electrolysis with green ammonia/methanol storage technologies, it represents China's first marine hydrogen demonstration project featuring offshore mobile platform-based green hydrogen production coupled with hydrogen-based chemical processes.<sup>244</sup>

## 6 Summary and outlook

Direct seawater electrolysis (DSE) presents a promising avenue for sustainable hydrogen production, leveraging abundant ocean resources to generate clean fuel. However, several stability challenges arise due to the complex composition of seawater, which includes various ions and microorganisms that can lead to chemical and physical degradation of the electrolysis system. Key issues include the degradation of traditional pure water electrolysis, competitive chlorine evolution reactions (CER), ion-induced precipitation, and biofouling, which damage electrodes and other components materials. These degradation processes can lead to reduced overall efficiency, limiting the longevity of the systems used for DSE.

In pursuit of longer-term stability, many catalysts have been tested in alkaline natural seawater and demonstrated significant performance, but there has been no further discussion on how these catalysts function in natural seawater. Compared to alkaline seawater solutions, natural seawater has lower conductivity, and its pH is closer to neutral or weakly alkaline. As a result, under the same conditions, NSE of DSE encounters a higher overpotential than ASE of DSE, making it difficult to achieve sufficient industrial-grade current density within the OER potential range at this pH. Additionally, due to the high overpotentials and the complex and harsh electrolyte environment of natural seawater, NSE electrodes are subjected to more intense chemical and electrochemical corrosion. It is important to note that the design of long-durability NSE cathodes also requires careful modulation around the key pH-related ion (OH<sup>-</sup>) and the development of NSE anode electrode catalytic materials requires greater emphasis on enhancing the water dissociation capability of electrocatalysts under neutral or weak alkaline conditions, improving OER selectivity and increasing the corrosion resistance of electrode materials. Generally, NSE exhibits poorer performance and durability compared to ASE and SSE. However, some high-performing catalysts provide effective guidance, such as the Cr<sub>2</sub>O<sub>3</sub>–CoO<sub>x</sub>, introducing a Lewis acid layer (Cr<sub>2</sub>O<sub>3</sub>) was introduced onto the catalyst surface (CoO<sub>x</sub>) to split H<sub>2</sub>O and generate localized surface alkalinity, thereby suppressing the release of chlorine gas captured at the anode. Additionally, the strong binding between OH<sup>-</sup> and the Lewis acid layer reduced the capture of OH<sup>-</sup> by Mg<sup>2+</sup> and Ca<sup>2+</sup> cations present in the seawater electrolyte, enabling anti-precipitation at the cathode.



Moreover, the design of electrolysis cells, whether membrane-less systems or membrane-based systems—plays a crucial role in enhancing operational stability. Membrane-less electrolyzers, leveraging hydrodynamic control (e.g., Segré–Silberberg effect, asymmetric electrodes) or capillary-fed designs, minimize gas crossover but face scalability limitations and require highly selective catalysts. Membrane-based systems, such as mature AMEWE, the stability of AEMs significantly impacts the long-term operation of DSE. Membrane degradation in DSE can be attributed to basic and seawater effects. Strategies to enhance membrane performance include developing robust high-molecular-weight polycarbazole membranes and blending ionomers that improve adhesion and ionic conductivity. Notable advances include hybrid MEA designs that strengthen bonding between catalyst layers and membranes. In addition, BPMWE have shown particular promise due to their ability to restrict chloride ion transport (achieving  $<0.005\% \text{ Cl}^-$  crossover), thereby minimizing corrosive side reactions. However, further optimization is still needed to adapt to asymmetric seawater feed to cross the laboratory to commercial level. For integrated systems, such as phase-transition PTFE membrane designs, demonstrate promise by combining *in situ* purification with electrolysis, achieving  $>3200$  hours of stable operation and  $>99.99\%$  impurity rejection. Moreover, it can be believed that the synergizing hydrogen production with byproduct valorization (e.g.,  $\text{Mg(OH)}_2$  for cement) could further enhance economic viability in the future.

Looking ahead, the future of DSE also aligns with the broader transition towards offshore renewable energy generation. The successful integration of advanced DSE technologies within maritime environments is pivotal. This will necessitate not only continued innovations in electrolysis cell designs and materials but also the establishment of robust support systems for hydrogen purification and transport. System-level integration—including consideration of auxiliary components like separators, compressors, and energy management systems—will be essential for maximizing efficiencies and ensuring reliable hydrogen production. With ongoing developments in offshore wind projects incentivizing hydrogen production directly at sea, three configurations (onshore, offshore, distributed) for hydrogen production using offshore electrolysis are compared. Although they have their pros and cons, there's significant potential for decentralized production capabilities to emerge, minimizing logistical barriers and improving economic viability. Several stability challenges arise in electrolysis systems due to the complex composition of seawater, intermittent fluctuations in renewable energy, and dynamic marine environmental disturbances, such as waves, temperature variations, and mechanical stresses. These factors can adversely affect the long-term stability of these systems, highlighting the need for innovations in dynamic control and buffering strategies: (1) to stabilize operating temperatures in offshore environments, it is essential to design integrated phase-change materials (PCMs) or incorporate active cooling and heating loops. (2) Additionally, real-time platform stabilization technologies, such as dynamic counterweight systems or thrusters, can mitigate wave-induced

oscillations, reducing mechanical stresses on electrolysis modules and gas–liquid separators. (3) Implementing hybrid energy storage solutions can buffer intermittent power inputs and minimize cycling degradation. (4) Real-time monitoring through embedded sensor networks will enable tracking of temperature variations and environmental changes, allowing for AI-driven predictive maintenance. (5) At the laboratory scale, we can pre-simulate waves, temperature variations, and conduct accelerated aging studies alongside intermittent power conditions. Characterizing electrode and membrane electrode assembly and linking them to electrochemical signals will contribute to building a database that enables AI-driven alarm signals to identify maintenance needs under actual operating conditions.

Overall, while the path to efficient and stable seawater electrolysis remains fraught with challenges, ongoing research and innovation position this technology as a central player in the quest for clean hydrogen production. By addressing the multifaceted aspects of stability and integration, DSE could potentially transform the renewable energy landscape and contribute substantially to global decarbonization efforts. Continued collaborative efforts among researchers, engineers, and industry stakeholders will be crucial to realizing the full potential of DSE in the near future.

## Data availability

This review paper does not contain any primary data generated or analyzed by the authors. All data discussed in this review are derived from previously published studies, which are appropriately cited in the manuscript. Readers are encouraged to refer to the original publications for detailed datasets and methodologies. If further information is required, the corresponding author is available for consultation and can provide guidance on accessing the referenced studies.

## Conflicts of interest

The authors declare no conflicts of interest.

## Acknowledgements

The work described in this paper was supported by a grant from the Research Grants Council of the Hong Kong Special Administrative Region, China (project no. 15308024), a grant from the Research Institute for Smart Energy at The Hong Kong Polytechnic University (CDB2) and a grant from Chongqing Talents (CSTB2024YCJH-KYXM0082).

## References

- W. Tong, M. Forster, F. Dionigi, S. Dresp, R. Sadeghi Erami, P. Strasser, A. J. Cowan and P. Farràs, *Nat. Energy*, 2020, **5**, 367–377.



2 D. Guan, B. Wang, J. Zhang, R. Shi, K. Jiao, L. Li, Y. Wang, B. Xie, Q. Zhang, J. Yu, Y. Zhu, Z. Shao and M. Ni, *Energy Environ. Sci.*, 2023, **16**, 4926–4943.

3 L. Wu, Z. Pan, S. Yuan, X. Shi, Y. Liu, F. Liu, X. Yan and L. An, *Chem. Eng. J.*, 2024, **488**, 151000.

4 L. Wu, G. Zhang, B. Xie, C. Tongsh and K. Jiao, *Int. J. Green Energy*, 2021, **18**, 541–555.

5 B. Zhang, C. Zhu, Z. Wu, E. Stavitski, Y. H. Lui, T.-H. Kim, H. Liu, L. Huang, X. Luan, L. Zhou, K. Jiang, W. Huang, S. Hu, H. Wang and J. S. Francisco, *Nano Lett.*, 2020, **20**, 136–144.

6 M. A. Achomo, A. Kumar, N. R. Peela and P. Muthukumar, *Int. J. Hydrogen Energy*, 2024, **58**, 1640–1672.

7 M. Aghaie, M. Mehrpooya and F. Pourfayaz, *Energy Convers. Manag.*, 2016, **124**, 141–154.

8 B. S. Zainal, P. J. Ker, H. Mohamed, H. C. Ong, I. M. R. Fattah, S. M. A. Rahman, L. D. Nghiem and T. M. I. Mahlia, *Renewable Sustainable Energy Rev.*, 2024, **189**, 113941.

9 L. Wu, Z. Pan, S. Yuan, X. Huo, Q. Zheng, X. Yan and L. An, *Energy AI*, 2024, **18**, 100411.

10 S. Yuan, C. Zhao, X. Cai, L. An, S. Shen, X. Yan and J. Zhang, *Prog. Energy Combust. Sci.*, 2023, **96**, 101075.

11 J. Guo, Y. Zheng, Z. Hu, C. Zheng, J. Mao, K. Du, M. Jaroniec, S.-Z. Qiao and T. Ling, *Nat. Energy*, 2023, **8**, 264–272.

12 S. Dresp, F. Dionigi, M. Klingenhof and P. Strasser, *ACS Energy Lett.*, 2019, **4**, 933–942.

13 Z. Zhu, L. Luo, Y. He, M. Mushtaq, J. Li, H. Yang, Z. Khanam, J. Qu, Z. Wang and M.-S. Balogun, *Adv. Funct. Mater.*, 2024, **34**, 2306061.

14 H. Yu, J. Wan, M. Goodsite and H. Jin, *One Earth*, 2023, **6**, 267–277.

15 S. Zhang, Y. Wang, S. Li, Z. Wang, H. Chen, L. Yi, X. Chen, Q. Yang, W. Xu, A. Wang and Z. Lu, *Nat. Commun.*, 2023, **14**, 4822.

16 W. He, X. Li, C. Tang, S. Zhou, X. Lu, W. Li, X. Li, X. Zeng, P. Dong, Y. Zhang and Q. Zhang, *ACS Nano*, 2023, **17**, 22227–22239.

17 J. Liang, Z. Li, X. He, Y. Luo, D. Zheng, Y. Wang, T. Li, B. Ying, S. Sun, Z. Cai, Q. Liu, B. Tang and X. Sun, *Mater. Today*, 2023, **69**, 193–235.

18 M. A. Khan, T. Al-Attas, S. Roy, M. M. Rahman, N. Ghaffour, V. Thangadurai, S. Larter, J. Hu, P. M. Ajayan and M. G. Kibria, *Energy Environ. Sci.*, 2021, **14**, 4831–4839.

19 J. Liu, S. Duan, H. Shi, T. Wang, X. Yang, Y. Huang, G. Wu and Q. Li, *Angew. Chem., Int. Ed.*, 2022, **134**, e202210753.

20 D. Liu, Y. Cai, X. Wang, Y. Zhuo, X. Sui, H. Pan and Z. Wang, *Energy Environ. Sci.*, 2024, **17**, 6897–6942.

21 C. Deng and G.-M. Weng, *Nano Energy*, 2024, **126**, 109674.

22 E. C. La Plante, X. Chen, S. Bustillos, A. Bouissonnie, T. Traynor, D. Jassby, L. Corsini, D. A. Simonetti and G. N. Sant, *ACS EST Eng.*, 2023, **3**, 955–968.

23 M. Qi, M. Qin, H. Wang, B. Lin, J. Chen, X. Shi, X. Du, S. Mao, J. Zhao, H. Zhang, L. Xi and Y. Wang, *Appl. Catal., B*, 2024, **356**, 124259.

24 Q. Chen, Y. Choo, N. Akther, H. K. Shon and G. Naidu, *Chem. Eng. J.*, 2024, **494**, 153007.

25 E. Jwa, W. Lee, S. Choi, Y.-C. Jeung, K. S. Hwang, J.-H. Han and N. Jeong, *Desalination*, 2024, **580**, 117580.

26 P. Farràs, P. Strasser and A. J. Cowan, *Joule*, 2021, **5**, 1921–1923.

27 B. A. Franco, P. Baptista, R. C. Neto and S. Ganilha, *Appl. Energy*, 2021, **286**, 116553.

28 H. Fei, R. Liu, T. Liu, M. Ju, J. Lei, Z. Wang, S. Wang, Y. Zhang, W. Chen, Z. Wu, M. Ni and J. Wang, *Adv. Mater.*, 2024, **36**, 2309211.

29 Y. Liu, Y. Wang, P. Fornasiero, G. Tian, P. Strasser and X.-Y. Yang, *Angew. Chem., Int. Ed.*, 2024, **136**, e202412087.

30 A. Badreldin, A. El Ghenemy, A.-R. Al-Zubi, A. Ashour, N. Hassan, A. Prakash, M. Kozusznik, D. V. Esposito, S. Ui Solim and A. Abdel-Wahab, *J. Power Sources*, 2024, **593**, 233991.

31 X. Zhou, G. Wei, C. Liu, Q. Zhao, H. Gao, W. Wang, X. Zhao, X. Zhao and H. Chen, *J. Colloid Interface Sci.*, 2024, **670**, 709–718.

32 C. Feng, M. Chen, Z. Yang, Z. Xie, X. Li, S. Li, A. Abudula and G. Guan, *J. Mater. Sci. Technol.*, 2023, **162**, 203–226.

33 D. H. Marin, J. T. Perryman, M. A. Hubert, G. A. Lindquist, L. Chen, A. M. Aleman, G. A. Kamat, V. A. Niemann, M. B. Stevens, Y. N. Regmi, S. W. Boettcher, A. C. Nielander and T. F. Jaramillo, *Joule*, 2023, **7**, 765–781.

34 H. Xie, Z. Zhao, T. Liu, Y. Wu, C. Lan, W. Jiang, L. Zhu, Y. Wang, D. Yang and Z. Shao, *Nature*, 2022, **612**, 673–678.

35 S. Ramakrishnan, M. Delpisheh, C. Convery, D. Niblett, M. Vinothkannan and M. Mamlouk, *Renewable Sustainable Energy Rev.*, 2024, **195**, 114320.

36 H. Meskher, A. R. Woldu, P. K. Chu, F. Lu and L. Hu, *EcoEnergy*, 2024, **2**, 630–651.

37 S. M. H. Hashemi, M. A. Modestino and D. Psaltis, *Energy Environ. Sci.*, 2015, **8**, 2003–2009.

38 H. Liu, M. Yu, X. Tong, Q. Wang and M. Chen, *Chem. Rev.*, 2024, **124**, 10509–10576.

39 T. Liu, Z. Zhao, W. Tang, Y. Chen, C. Lan, L. Zhu, W. Jiang, Y. Wu, Y. Wang, Z. Yang, D. Yang, Q. Wang, L. Luo, T. Liu and H. Xie, *Nat. Commun.*, 2024, **15**, 5305.

40 D. Niblett, M. Delpisheh, S. Ramakrishnan and M. Mamlouk, *J. Power Sources*, 2024, **592**, 233904.

41 R. d'Amore-Domenech and T. J. Leo, *ACS Sustainable Chem. Eng.*, 2019, **7**, 8006–8022.

42 J. Shi, R. Xia, X. Zheng, R. Yao and J. Zheng, *A Review on Hydrogen Production From Ocean Renewable Energy and the Application Status*, 2023.

43 L. Ai, Y. Tian, T. Xiao, J. Zhang, C. Zhang and J. Jiang, *J. Colloid Interface Sci.*, 2024, **673**, 607–615.

44 L. Chen, C. Yu, J. Dong, Y. Han, H. Huang, W. Li, Y. Zhang, X. Tan and J. Qiu, *Chem. Soc. Rev.*, 2024, **53**, 7455–7488.

45 Y. Wang, M. Wang, Y. Yang, D. Kong, C. Meng, D. Zhang, H. Hu and M. Wu, *Chem. Catal.*, 2023, **3**, 100643.

46 F. Dionigi, T. Reier, Z. Pawolek, M. Glielch and P. Strasser, *ChemSusChem*, 2016, **9**, 962–972.

47 J. S. Ko, J. K. Johnson, P. I. Johnson and Z. Xia, *Chem-CatChem*, 2020, **12**, 4526–4532.



48 J. Chang and Y. Yang, *Renewables*, 2023, **1**, 415–454.

49 L. Yu, Q. Zhu, S. Song, B. McElhenny, D. Wang, C. Wu, Z. Qin, J. Bao, Y. Yu, S. Chen and Z. Ren, *Nat. Commun.*, 2019, **10**, 5106.

50 J. Corbin, M. Jones, C. Lyu, A. Loh, Z. Zhang, Y. Zhu and X. Li, *RSC Adv.*, 2024, **14**, 6416–6442.

51 W. Zheng, L. Y. S. Lee and K.-Y. Wong, *Nanoscale*, 2021, **13**, 15177–15187.

52 M. Chatenet, B. G. Pollet, D. R. Dekel, F. Dionigi, J. Deseure, P. Millet, R. D. Braatz, M. Z. Bazant, M. Eikerling, I. Staffell, P. Balcombe, Y. Shao-Horn and H. Schäfer, *Chem. Soc. Rev.*, 2022, **51**, 4583–4762.

53 X.-J. Zhai, Q.-X. Lv, J.-Y. Xie, Y.-X. Zhang, Y.-M. Chai and B. Dong, *Chem. Eng. J.*, 2024, 153187.

54 J. Yu, B.-Q. Li, C.-X. Zhao and Q. Zhang, *Energy Environ. Sci.*, 2020, **13**, 3253–3268.

55 B. Xu, J. Liang, X. Sun and X. Xiong, *Green Chem.*, 2023, **25**, 3767–3790.

56 N.-T. Suen, S.-F. Hung, Q. Quan, N. Zhang, Y.-J. Xu and H. M. Chen, *Chem. Soc. Rev.*, 2017, **46**, 337–365.

57 F. Meharban, C. Lin, X. Wu, L. Tan, H. Wang, W. Hu, D. Zhou, X. Li and W. Luo, *Adv. Energy Mater.*, 2024, **14**, 2402886.

58 J. Niklas Hausmann, R. Schlögl, P. W. Menezes and M. Driess, *Energy Environ. Sci.*, 2021, **14**, 3679–3685.

59 C. Yang, G. Rousse, K. Louise Svane, P. E. Pearce, A. M. Abakumov, M. Deschamps, G. Cibin, A. V. Chadwick, D. A. Dalla Corte, H. Anton Hansen, T. Vegge, J.-M. Tarascon and A. Grimaud, *Nat. Commun.*, 2020, **11**, 1378.

60 S. M. Hoseinieh, F. Ashrafizadeh and M. H. Maddahi, *J. Electrochem. Soc.*, 2010, **157**, E50.

61 Y. Hu, M. Tu, T. Xiong, Y. He, M. Mushtaq, H. Yang, Z. Khanam, Y. Huang, J. Deng and M.-S. Balogun, *J. Energy Chem.*, 2025, **103**, 282–293.

62 Y.-Y. Ma, C.-X. Wu, X.-J. Feng, H.-Q. Tan, L.-K. Yan, Y. Liu, Z.-H. Kang, E.-B. Wang and Y.-G. Li, *Energy Environ. Sci.*, 2017, **10**, 788–798.

63 X. Wu, S. Zhou, Z. Wang, J. Liu, W. Pei, P. Yang, J. Zhao and J. Qiu, *Adv. Energy Mater.*, 2019, **9**, 1901333.

64 M. Auinger, I. Katsounaros, J. C. Meier, S. O. Klemm, P. U. Biedermann, A. A. Topalov, M. Rohwerder and K. J. J. Mayrhofer, *Phys. Chem. Chem. Phys.*, 2011, **13**, 16384–16394.

65 L. Yu, Q. Zhu, S. Song, B. McElhenny, D. Wang, C. Wu, Z. Qin, J. Bao, Y. Yu, S. Chen and Z. Ren, *Nat. Commun.*, 2019, **10**, 5106.

66 X. Lu, J. Pan, E. Lovell, T. H. Tan, Y. H. Ng and R. Amal, *Energy Environ. Sci.*, 2018, **11**, 1898–1910.

67 S. Dresp, F. Dionigi, S. Loos, J. Ferreira de Araujo, C. Spöri, M. Gliech, H. Dau and P. Strasser, *Adv. Energy Mater.*, 2018, **8**, 1800338.

68 H. Jin, J. Wang, L. Tian, M. Gao, J. Zhao and L. Ren, *Mater. Des.*, 2022, **213**, 110307.

69 D. M. Yebra, S. Kiil and K. Dam-Johansen, *Prog. Org. Coat.*, 2004, **50**, 75–104.

70 Y. Li and C. Ning, *Bioact. Mater.*, 2019, **4**, 189–195.

71 I. G. Wenten, M. Z. Bazant and K. Khoiruddin, *Sep. Purif. Technol.*, 2024, **345**, 127228.

72 W. Zheng, M. Liu and L. Y. S. Lee, *ACS Catal.*, 2020, **10**, 81–92.

73 N. Rajapakse, M. Zargar, T. Sen and M. Khiadani, *Sep. Purif. Technol.*, 2022, **289**, 120772.

74 J. Das, S. Mandal, A. Borbora, S. Rani, M. Tenjimbayashi and U. Manna, *Adv. Funct. Mater.*, 2024, **34**, 2311648.

75 P. A. Kempler, R. H. Coridan and L. Luo, *Chem. Rev.*, 2024, **124**, 10964–11007.

76 A. W. Tricker, J. K. Lee, J. R. Shin, N. Danilovic, A. Z. Weber and X. Peng, *J. Power Sources*, 2023, **567**, 232967.

77 M. B. Poudel, N. Logeshwaran, S. Prabhakaran, A. R. Kim, D. H. Kim and D. J. Yoo, *Adv. Mater.*, 2024, **36**, 2305813.

78 J. Zheng, *Appl. Surf. Sci.*, 2017, **413**, 72–82.

79 X. Ju, H. Guo, Z. Tao, A. Niu, H. Wei, J. S. Chen, X. He, H. Xian, X. Sun, Q. Kong and T. Li, *J. Colloid Interface Sci.*, 2025, **683**, 189–196.

80 P. Gu, Y. Song, Y. Fan, X. Meng, J. Liu, G. Wang, Z. Li, H. Sun, Z. Zhao and J. Zou, *Adv. Energy Mater.*, 2024, 2403657.

81 Y. Zhang, S. Jeong, E. Son, Y. Choi, S. Lee, J. M. Baik and H. Park, *ACS Nano*, 2024, **18**, 16312–16323.

82 F. Liu, R. Hu, H. Qiu, H. Miao, Q. Wang and J. Yuan, *J. Alloys Compd.*, 2022, **913**, 165342.

83 S. A. Patil, A. C. Khot, V. D. Chavan, I. Rabani, D. Kim, J. Jung, H. Im and N. K. Shrestha, *Chem. Eng. J.*, 2024, **480**, 146545.

84 Y. Kuang, M. J. Kenney, Y. Meng, W.-H. Hung, Y. Liu, J. E. Huang, R. Prasanna, P. Li, Y. Li, L. Wang, M.-C. Lin, M. D. McGehee, X. Sun and H. Dai, *Proc. Natl. Acad. Sci. U. S. A.*, 2019, **116**, 6624–6629.

85 R. Andaveh, A. Sabour Rouhaghdam, J. Ai, M. Maleki, K. Wang, A. Seif, G. Barati Darband and J. Li, *Appl. Catal., B*, 2023, **325**, 122355.

86 C. Huang, Q. Zhou, L. Yu, D. Duan, T. Cao, S. Qiu, Z. Wang, J. Guo, Y. Xie, L. Li and Y. Yu, *Adv. Energy Mater.*, 2023, **13**, 2301475.

87 X. Kang, F. Yang, Z. Zhang, H. Liu, S. Ge, S. Hu, S. Li, Y. Luo, Q. Yu, Z. Liu, Q. Wang, W. Ren, C. Sun, H.-M. Cheng and B. Liu, *Nat. Commun.*, 2023, **14**, 3607.

88 L. Zhou, Z.-H. Huang, F. Kang and R. Lv, *Chem. Eng. J.*, 2023, **458**, 141457.

89 H. Zhang, Z. Bi, P. Sun, A. Chen, T. Wågberg, X. Hu, X. Liu, L. Jiang and G. Hu, *ACS Nano*, 2023, **17**, 16008–16019.

90 J.-T. Ren, L. Chen, W.-W. Tian, X.-L. Song, Q.-H. Kong, H.-Y. Wang and Z.-Y. Yuan, *Small*, 2023, **19**, 2300194.

91 L. Yu, Q. Zhu, S. Song, B. McElhenny, D. Wang, C. Wu, Z. Qin, J. Bao, Y. Yu, S. Chen and Z. Ren, *Nat. Commun.*, 2019, **10**, 5106.

92 X. Liu, Q. Yu, X. Qu, X. Wang, J. Chi and L. Wang, *Adv. Mater.*, 2024, **36**, 2307395.

93 T. Cui, J. Chi, K. Liu, J. Zhu, L. Guo, H. Mao, X. Liu, J. Lai, H. Guo and L. Wang, *Appl. Catal., B*, 2024, **357**, 124269.

94 Z. Li, Y. Yao, S. Sun, J. Liang, S. Hong, H. Zhang, C. Yang, X. Zhang, Z. Cai, J. Li, Y. Ren, Y. Luo, D. Zheng, X. He,



Q. Liu, Y. Wang, F. Gong, X. Sun and B. Tang, *Angew. Chem., Int. Ed.*, 2024, **63**, e202316522.

95 L. Yu, J. Xiao, C. Huang, J. Zhou, M. Qiu, Y. Yu, Z. Ren, C.-W. Chu and J. C. Yu, *Proc. Natl. Acad. Sci. U. S. A.*, 2022, **119**, e2202382119.

96 W. Ma, D. Li, L. Liao, H. Zhou, F. Zhang, X. Zhou, Y. Mo and F. Yu, *Small*, 2023, **19**, 2207082.

97 D. Wu, B. Liu, R. Li, D. Chen, W. Zeng, H. Zhao, Y. Yao, R. Qin, J. Yu, L. Chen, J. Zhang, B. Li and S. Mu, *Small*, 2023, **19**, 2300030.

98 F. Zhang, Y. Liu, F. Yu, H. Pang, X. Zhou, D. Li, W. Ma, Q. Zhou, Y. Mo and H. Zhou, *ACS Nano*, 2023, **17**, 1681–1692.

99 Y. S. Park, J. Lee, M. J. Jang, J. Yang, J. Jeong, J. Park, Y. Kim, M. H. Seo, Z. Chen and S. M. Choi, *J. Mater. Chem. A*, 2021, **9**, 9586–9592.

100 Y. Wang, W. Yu, B. Zhou, W. Xiao, J. Wang, X. Wang, G. Xu, B. Li, Z. Li, Z. Wu and L. Wang, *J. Mater. Chem. A*, 2023, **11**, 1886–1893.

101 L. Yu, L. Wu, B. McElhenny, S. Song, D. Luo, F. Zhang, Y. Yu, S. Chen and Z. Ren, *Energy Environ. Sci.*, 2020, **13**, 3439–3446.

102 L. Wu, L. Yu, F. Zhang, B. McElhenny, D. Luo, A. Karim, S. Chen and Z. Ren, *Adv. Funct. Mater.*, 2021, **31**, 2006484.

103 T. Ma, W. Xu, B. Li, X. Chen, J. Zhao, S. Wan, K. Jiang, S. Zhang, Z. Wang, Z. Tian, Z. Lu and L. Chen, *Angew. Chem., Int. Ed.*, 2021, **60**, 22740–22744.

104 X. Duan, Q. Sha, P. Li, T. Li, G. Yang, W. Liu, E. Yu, D. Zhou, J. Fang, W. Chen, Y. Chen, L. Zheng, J. Liao, Z. Wang, Y. Li, H. Yang, G. Zhang, Z. Zhuang, S.-F. Hung, C. Jing, J. Luo, L. Bai, J. Dong, H. Xiao, W. Liu, Y. Kuang, B. Liu and X. Sun, *Nat. Commun.*, 2024, **15**, 1973.

105 N. Wang, P. Ou, S.-F. Hung, J. E. Huang, A. Ozden, J. Abed, I. Grigioni, C. Chen, R. K. Miao, Y. Yan, J. Zhang, Z. Wang, R. Dorakhan, A. Badreldin, A. Abdel-Wahab, D. Sinton, Y. Liu, H. Liang and E. H. Sargent, *Adv. Mater.*, 2023, **35**, 2210057.

106 W.-H. Hung, B.-Y. Xue, T.-M. Lin, S.-Y. Lu and I.-Y. Tsao, *Mater. Today Energy*, 2021, **19**, 100575.

107 H. Sun, J. Sun, Y. Song, Y. Zhang, Y. Qiu, M. Sun, X. Tian, C. Li, Z. Lv and L. Zhang, *ACS Appl. Mater. Interfaces*, 2022, **14**, 22061–22070.

108 L. Shao, X. Han, L. Shi, T. Wang, Y. Zhang, Z. Jiang, Z. Yin, X. Zheng, J. Li, X. Han and Y. Deng, *Adv. Energy Mater.*, 2024, **14**, 2303261.

109 K. Huang, H. Qi, W. Zeng, L. Guo, C. Lian, H. Liu and J. Hu, *Sep. Purif. Technol.*, 2025, **364**, 132364.

110 J. Mu, C. Yu, X. Song, L. Chen, J. Zhao and J. Qiu, *Adv. Funct. Mater.*, 2025, 2423965.

111 H. Jin, X. Liu, A. Vasileff, Y. Jiao, Y. Zhao, Y. Zheng and S.-Z. Qiao, *ACS Nano*, 2018, **12**, 12761–12769.

112 L. Xiu, W. Pei, S. Zhou, Z. Wang, P. Yang, J. Zhao and J. Qiu, *Adv. Funct. Mater.*, 2020, **30**, 1910028.

113 Y. Zhang, P. Li, X. Yang, W. Fa and S. Ge, *J. Alloys Compd.*, 2018, **732**, 248–256.

114 Q. Lv, J. Han, X. Tan, W. Wang, L. Cao and B. Dong, *ACS Appl. Energy Mater.*, 2019, **2**, 3910–3917.

115 S. Ye, W. Xiong, P. Liao, L. Zheng, X. Ren, C. He, Q. Zhang and J. Liu, *J. Mater. Chem. A*, 2020, **8**, 11246–11254.

116 Y. Huang, L. Hu, R. Liu, Y. Hu, T. Xiong, W. Qiu, M.-S. Jie, T. Balogun, A. Pan and Y. Tong, *Appl. Catal., B*, 2019, **251**, 181–194.

117 H. Li, Q. Tang, B. He and P. Yang, *J. Mater. Chem. A*, 2016, **4**, 6513–6520.

118 N. Nie, D. Zhang, Z. Wang, W. Yu, S. Ge, J. Xiong, Y. Gu, B. Yang, J. Lai and L. Wang, *Appl. Catal., B*, 2022, **318**, 121808.

119 D. Bao, L. Huang, Y. Gao, K. Davey, Y. Zheng and S.-Z. Qiao, *J. Am. Chem. Soc.*, 2024, **146**, 34711–34719.

120 Q. Sha, S. Wang, L. Yan, Y. Feng, Z. Zhang, S. Li, X. Guo, T. Li, H. Li, Z. Zhuang, D. Zhou, B. Liu and X. Sun, *Nature*, 2025, **639**, 360–367.

121 J. Zhu, J. Chi, T. Cui, L. Guo, S. Wu, B. Li, J. Lai and L. Wang, *Appl. Catal., B*, 2023, **328**, 122487.

122 W. Xu, T. Ma, H. Chen, D. Pan, Z. Wang, S. Zhang, P. Zhang, S. Bao, Q. Yang, L. Zhou, Z. Tian, S. Dai and Z. Lu, *Adv. Funct. Mater.*, 2023, **33**, 2302263.

123 X. Gu, M. Yu, S. Chen, X. Mu, Z. Xu, W. Shao, J. Zhu, C. Chen, S. Liu and S. Mu, *Nano Energy*, 2022, **102**, 107656.

124 H. Hu, Z. Zhang, Y. Zhang, T. Thomas, H. Du, K. Huang, J. P. Attfield and M. Yang, *Energy Environ. Sci.*, 2023, **16**, 4584–4592.

125 S. Li, Y. Zhuo, D. Liu, H. Pan and Z. Wang, *Appl. Catal., B*, 2024, **355**, 124188.

126 M. Ning, Y. Wang, L. Wu, L. Yang, Z. Chen, S. Song, Y. Yao, J. Bao, S. Chen and Z. Ren, *Nano-Micro Lett.*, 2023, **15**, 157.

127 H. Hu, Z. Zhang, L. Liu, X. Che, J. Wang, Y. Zhu, J. P. Attfield and M. Yang, *Sci. Adv.*, 2024, **10**, eadn7012.

128 S. Jeong, U. Kim, S. Lee, Y. Zhang, E. Son, K.-J. Choi, Y.-K. Han, J. M. Baik and H. Park, *ACS Nano*, 2024, **18**, 7558–7569.

129 J. Lu, S. Chen, Y. Zhuo, X. Mao, D. Liu and Z. Wang, *Adv. Funct. Mater.*, 2023, **33**, 2308191.

130 M. Wen, Y. Cao, B. Wu, T. Xiao, R. Cao, Q. Wang, X. Liu, H. Xue, Y. Yu, J. Lin, C. Xu, J. Xu and B. OuYang, *Nat. Commun.*, 2021, **12**, 5106.

131 H. Zhang, J. Diao, M. Ouyang, H. Yadegari, M. Mao, M. Wang, G. Henkelman, F. Xie and D. J. Riley, *ACS Catal.*, 2023, **13**, 1349–1358.

132 Y. Yu, W. Zhou, X. Zhou, J. Yuan, X. Zhang, L. Wang, J. Li, X. Meng, F. Sun, J. Gao and G. Zhao, *ACS Catal.*, 2024, **14**, 18322–18332.

133 T. Zhao, S. Wang, C. Jia, C. Rong, Z. Su, K. Dastafkan, Q. Zhang and C. Zhao, *Small*, 2023, **19**, 2208076.

134 J. Fan, X. Ma, J. Xia, L. Zhang, Q. Bi and W. Hao, *J. Colloid Interface Sci.*, 2024, **657**, 393–401.

135 H. Jin, X. Wang, C. Tang, A. Vasileff, L. Li, A. Slattery and S.-Z. Qiao, *Adv. Mater.*, 2021, **33**, 2007508.

136 H.-M. Zhang, Y. Gao, J. Li, J. Sun, D. Wang, L. Wang and Y. Meng, *Fuel*, 2024, **375**, 132652.

137 Z. Kato, M. Sato, Y. Sasaki, K. Izumiya, N. Kumagai and K. Hashimoto, *Electrochim. Acta*, 2014, **116**, 152–157.



138 N. Jiang and H. Meng, *Surf. Coat. Technol.*, 2012, **206**, 4362–4367.

139 K. Jiang, W. Liu, W. Lai, M. Wang, Q. Li, Z. Wang, J. Yuan, Y. Deng, J. Bao and H. Ji, *Inorg. Chem.*, 2021, **60**, 17371–17378.

140 P. Gayen, S. Saha and V. Ramani, *ACS Appl. Energy Mater.*, 2020, **3**, 3978–3983.

141 X. Xu, Y. Pan, Y. Zhong, C. Shi, D. Guan, L. Ge, Z. Hu, Y.-Y. Chin, H.-J. Lin, C.-T. Chen, H. Wang, S. P. Jiang and Z. Shao, *Adv. Sci.*, 2022, **9**, 2200530.

142 R. Fan, C. Liu, Z. Li, H. Huang, J. Feng, Z. Li and Z. Zou, *Nat. Sustain.*, 2024, **7**, 158–167.

143 W. Liu, J. Yu, M. G. Sendeku, T. Li, W. Gao, G. Yang, Y. Kuang and X. Sun, *Angew. Chem., Int. Ed.*, 2023, **62**, e202309882.

144 Z. Gong, J. Liu, M. Yan, H. Gong, G. Ye and H. Fei, *ACS Nano*, 2023, **17**, 18372–18381.

145 S. Zhang, Y. Wang, X. Wei, L. Chu, W. Tian, H. Wang and M. Huang, *Appl. Catal., B*, 2023, **336**, 122926.

146 K. Obata and K. Takanabe, *Angew. Chem., Int. Ed.*, 2018, **130**, 1632–1636.

147 T. P. Keane, S. S. Veroneau, A. C. Hartnett and D. G. Nocera, *J. Am. Chem. Soc.*, 2023, **145**, 4989–4993.

148 B. Wang, M. Lu, D. Chen, Q. Zhang, W. Wang, Y. Kang, Z. Fang, G. Pang and S. Feng, *J. Mater. Chem. A*, 2021, **9**, 13562–13569.

149 J. Tang, C. Su and Z. Shao, *Exploration*, 2024, **4**, 20220112.

150 L. Shao, X. Han, L. Shi, T. Wang, Y. Zhang, Z. Jiang, Z. Yin, X. Zheng, J. Li, X. Han and Y. Deng, *Adv. Energy Mater.*, 2024, **14**, 2303261.

151 J. Na, H. Yu, S. Jia, J. Chi, K. Lv, T. Li, Y. Zhao, Y. Zhao, H. Zhang and Z. Shao, *J. Energy Chem.*, 2024, **91**, 370–382.

152 M. L. Frisch, T. N. Thanh, A. Arinchtein, L. Hager, J. Schmidt, S. Brückner, J. Kerres and P. Strasser, *ACS Energy Lett.*, 2023, **8**, 2387–2394.

153 P. Li, S. Zhao, Y. Huang, Q. Huang, Y. Yang and H. Yang, *ACS Catal.*, 2023, **13**, 15360–15374.

154 T. Kou, S. Wang, R. Shi, T. Zhang, S. Chiovoloni, J. Q. Lu, W. Chen, M. A. Worsley, B. C. Wood, S. E. Baker, E. B. Duoss, R. Wu, C. Zhu and Y. Li, *Adv. Energy Mater.*, 2020, **10**, 2002955.

155 D. Liu, X. Wei, J. Lu, X. Wang, K. Liu, Y. Cai, Y. Qi, L. Wang, H. Ai and Z. Wang, *Adv. Mater.*, 2024, **36**, 2408982.

156 J. Liang, Z. Cai, X. He, Y. Luo, D. Zheng, S. Sun, Q. Liu, L. Li, W. Chu, S. Alfaifi, F. Luo, Y. Yao, B. Tang and X. Sun, *Chem.*, 2024, **10**, 3067–3087.

157 Q. Liu, Z. Yan, J. Gao, H. Fan, M. Li and E. Wang, *Chem. Sci.*, 2023, **14**, 11830–11839.

158 L. Wan, J. Liu, D. Lin, Z. Xu, Y. Zhen, M. Pang, Q. Xu and B. Wang, *Energy Environ. Sci.*, 2024, **17**, 3396–3408.

159 C. Hu, Y. J. Lee, Y. Ma, X. Zhang, S. W. Jung, H. Hwang, H. K. Cho, M.-G. Kim, S. J. Yoo, Q. Zhang and Y. M. Lee, *ACS Energy Lett.*, 2024, **9**, 1219–1227.

160 D. V. Esposito, *Joule*, 2017, **1**, 651–658.

161 M. I. Gillespie, F. van der Merwe and R. J. Kriek, *J. Power Sources*, 2015, **293**, 228–235.

162 G. D. O’Neil, C. D. Christian, D. E. Brown and D. V. Esposito, *J. Electrochem. Soc.*, 2016, **163**, F3012–F3019.

163 J. T. Davis, J. Qi, X. Fan, J. C. Bui and D. V. Esposito, *Int. J. Hydrogen Energy*, 2018, **43**, 1224–1238.

164 B. S. De, P. Kumar, N. Khare, J.-L. Luo, A. Elias and S. Basu, *ACS Appl. Energy Mater.*, 2021, **4**, 9639–9652.

165 A. Hodges, A. L. Hoang, G. Tsekouras, K. Wagner, C.-Y. Lee, G. F. Swiegers and G. G. Wallace, *Nat. Commun.*, 2022, **13**, 1304.

166 S. Dresp, T. N. Thanh, M. Klingenhofer, S. Brückner, P. Hauke and P. Strasser, *Energy Environ. Sci.*, 2020, **13**, 1725–1729.

167 Q. Xu, L. Zhang, J. Zhang, J. Wang, Y. Hu, H. Jiang and C. Li, *EnergyChem*, 2022, **4**, 100087.

168 X. Duan, X. Xiang, J. Chen, A. Zhou, J. Xiao, J. Wen and S. Wang, *Int. J. Hydrogen Energy*, 2024, **55**, 1505–1513.

169 H. Shi, T. Wang, J. Liu, W. Chen, S. Li, J. Liang, S. Liu, X. Liu, Z. Cai, C. Wang, D. Su, Y. Huang, L. Elbaz and Q. Li, *Nat. Commun.*, 2023, **14**, 3934.

170 T. Liu, C. Lan, M. Tang, M. Li, Y. Xu, H. Yang, Q. Deng, W. Jiang, Z. Zhao, Y. Wu and H. Xie, *Nat. Commun.*, 2024, **15**, 8874.

171 S. Kumari, R. Turner White, B. Kumar and J. M. Spurgeon, *Energy Environ. Sci.*, 2016, **9**, 1725–1733.

172 R. Rossi, D. M. Hall, L. Shi, N. R. Cross, C. A. Gorski, M. A. Hickner and B. E. Logan, *Energy Environ. Sci.*, 2021, **14**, 6041–6049.

173 J.-H. Han, *J. Electrochem. Soc.*, 2023, **170**, 093506.

174 L. Wu, L. An, D. Jiao, Y. Xu, G. Zhang and K. Jiao, *Appl. Energy*, 2022, **323**, 119651.

175 R. Yoshimura, S. Wai, Y. Ota, K. Nishioka and Y. Suzuki, *Catalysts*, 2022, **12**, 934.

176 J. Li, J. Sun, Z. Li and X. Meng, *Int. J. Hydrogen Energy*, 2022, **47**, 29685–29697.

177 S. Z. Oener, M. J. Foster and S. W. Boettcher, *Science*, 2020, **369**, 1099–1103.

178 M. A. Blommaert, J. A. H. Verdonk, H. C. B. Blommaert, W. A. Smith and D. A. Vermaas, *ACS Appl. Energy Mater.*, 2020, **3**, 5804–5812.

179 B. Kim, H. K. Shon, D. S. Han and H. Park, *Desalination*, 2023, **551**, 116431.

180 J.-H. Han, *ChemSusChem*, 2022, **15**, e202200372.

181 G. Moon, J. Lim, B. Kim, D. S. Han and H. Park, *Green Chem.*, 2025, **27**, 982–1005.

182 A. Zhegur, N. Gjineci, S. Willdorf-Cohen, A. N. Mondal, C. E. Diesendruck, N. Gavish and D. R. Dekel, *ACS Appl. Polym. Mater.*, 2020, **2**, 360–367.

183 G. A. Lindquist, Q. Xu, S. Z. Oener and S. W. Boettcher, *Joule*, 2020, **4**, 2549–2561.

184 S. Kim, S. H. Yang, S.-H. Shin, H. J. Cho, J. K. Jang, T. H. Kim, S.-G. Oh, T.-H. Kim, H. Han and J. Y. Lee, *Energy Environ. Sci.*, 2024, **17**, 5399–5409.

185 Y. Zheng, W. Ma, A. Serban, A. Allushi and X. Hu, *Angew. Chem., Int. Ed.*, 2025, **64**, e202413698.

186 L. Li, C. Lin, X. Ma, Y. Ma, A. Zhu, Z. Xie and Q. Zhang, *Chem. Eng. J.*, 2025, **508**, 160916.



187 H. Becker, J. Murawski, D. V. Shinde, I. E. L. Stephens, G. Hinds and G. Smith, *Sustainable Energy Fuels*, 2023, **7**, 1565–1603.

188 H. Saada, B. Fabre, G. Loget and G. Benoit, *ACS Energy Lett.*, 2024, **9**, 3351–3368.

189 Y. Zheng, A. Serban, H. Zhang, N. Chen, F. Song and X. Hu, *ACS Energy Lett.*, 2023, **8**, 5018–5024.

190 W. Zhang, M. Liu, X. Gu, Y. Shi, Z. Deng and N. Cai, *Chem. Rev.*, 2023, **123**, 7119–7192.

191 C. K. Lim, Q. Liu, J. Zhou, Q. Sun and S. H. Chan, *J. Power Sources*, 2017, **342**, 79–87.

192 Z. Liu, B. Han, Z. Lu, W. Guan, Y. Li, C. Song, L. Chen and S. C. Singhal, *Appl. Energy*, 2021, **300**, 117439.

193 J. P. Stempien, Q. Liu, M. Ni, Q. Sun and S. H. Chan, *Electrochim. Acta*, 2014, **147**, 490–497.

194 A. Hauch, R. Küngas, P. Blennow, A. B. Hansen, J. B. Hansen, B. V. Mathiesen and M. B. Mogensen, *Science*, 2020, **370**, eaba6118.

195 S. S. Veroneau, A. C. Hartnett, A. E. Thorarinsdottir and D. G. Nocera, *ACS Appl. Energy Mater.*, 2022, **5**, 1403–1408.

196 S. S. Veroneau and D. G. Nocera, *Proc. Natl. Acad. Sci. U. S. A.*, 2021, **118**, e2024855118.

197 B. E. Logan, L. Shi and R. Rossi, *Joule*, 2021, **5**, 760–762.

198 H. Jin, J. Xu, H. Liu, H. Shen, H. Yu, M. Jaroniec, Y. Zheng and S.-Z. Qiao, *Sci. Adv.*, 2023, **9**, eadi7755.

199 Q.-Y. Fang, J.-J. Gu, R.-X. He, W.-W. Ni, J. Ran, N. Deng and J.-B. He, *J. Solid State Electrochem.*, 2025, 1–9.

200 O. Horner, D. P. Wilkinson and E. L. Gyenge, *J. Electrochem. Soc.*, 2024, **171**, 094502.

201 K. Kishor, S. Saha, A. Parashtekar and R. G. S. Pala, *J. Electrochem. Soc.*, 2018, **165**, J3276–J3280.

202 A. Mayyas, M. Ruth, B. Pivovar, G. Bender and K. Wipke, *Manufacturing Cost Analysis for Proton Exchange Membrane Water Electrolyzers*, 2019.

203 X. Lyu, J. Li, C. J. Jafta, Y. Bai, C. P. Canales, F. Magnus, Á. S. Ingason and A. Serov, *J. Environ. Chem. Eng.*, 2022, **10**, 108486.

204 H. Hu, X. Wang, J. P. Attfield and M. Yang, *Chem. Soc. Rev.*, 2024, **53**, 163–203.

205 X. Lyu, Y. Bai, J. Li, R. Tao, J. Yang and A. Serov, *J. Environ. Chem. Eng.*, 2023, **11**, 109667.

206 J. Wang, L. Ji and Z. Chen, *ACS Catal.*, 2016, **6**, 6987–6992.

207 S. Mitchell, N.-L. Michels and J. Pérez-Ramírez, *Chem. Soc. Rev.*, 2013, **42**, 6094.

208 S. Hsu, J. Miao, L. Zhang, J. Gao, H. Wang, H. Tao, S. Hung, A. Vasileff, S. Z. Qiao and B. Liu, *Adv. Mater.*, 2018, **30**, 1707261.

209 Y. Zhao, B. Jin, A. Vasileff, Y. Jiao and S.-Z. Qiao, *J. Mater. Chem. A*, 2019, **7**, 8117–8121.

210 S. Wang, P. Yang, X. Sun, H. Xing, J. Hu, P. Chen, Z. Cui, W. Zhu and Z. Ma, *Appl. Catal., B*, 2021, **297**, 120386.

211 L. Wu, F. Zhang, S. Song, M. Ning, Q. Zhu, J. Zhou, G. Gao, Z. Chen, Q. Zhou, X. Xing, T. Tong, Y. Yao, J. Bao, L. Yu, S. Chen and Z. Ren, *Adv. Mater.*, 2022, **34**, 2201774.

212 S. Seenivasan and D.-H. Kim, *J. Mater. Chem. A*, 2022, **10**, 9547–9564.

213 W. Xu, Z. Wang, P. Liu, X. Tang, S. Zhang, H. Chen, Q. Yang, X. Chen, Z. Tian, S. Dai, L. Chen and Z. Lu, *Adv. Mater.*, 2024, **36**, 2306062.

214 B. C. M. Martindale and E. Reisner, *Adv. Energy Mater.*, 2016, **6**, 1502095.

215 J. Chang, G. Wang, Z. Yang, B. Li, Q. Wang, R. Kulieev, N. Orlovskaya, M. Gu, Y. Du, G. Wang and Y. Yang, *Adv. Mater.*, 2021, **33**, 2101425.

216 J.-H. Han, E. Jwa, H. Lee, E. J. Kim, J.-Y. Nam, K. S. Hwang, N. Jeong, J. Choi, H. Kim, Y.-C. Jeung and T. D. Chung, *Chem. Eng. J.*, 2022, **429**, 132383.

217 A. Surbled, N. Larché and D. Thierry, *Corrosion Management of Seawater Cooling Systems*, Elsevier, 2024, pp. 67–128.

218 D. A. Shifler, *LaQue's Handbook of Marine Corrosion*, John Wiley & Sons, Ltd, 2022, pp. 667–689.

219 A. Banerjee and B. K. Banerjee, in 2015 International Conference on Sustainable Mobility Applications, Renewables and Technology (SMART), 2015, pp. 1–12.

220 T. Matos, V. C. Pinto, P. J. Sousa, M. S. Martins, E. Fernández and L. M. Goncalves, *Chem. Eng. J.*, 2024, **500**, 156836.

221 H. Guosheng, X. Lukuo, L. Xiangbo and W. Hongren, *Int. J. Electrochem. Sci.*, 2016, **11**, 8738–8748.

222 K. Xu, J. Tian, S. Xie and P. Wu, *J. Therm. Spray Technol.*, 2023, **32**, 2170–2186.

223 X. Shi, H. Liang and Y. Li, *Coatings*, 2024, **14**, 1454.

224 S. Pourhashem, A. Seif, F. Saba, E. G. Nezhad, X. Ji, Z. Zhou, X. Zhai, M. Mirzaee, J. Duan, A. Rashidi and B. Hou, *J. Mater. Sci. Technol.*, 2022, **118**, 73–113.

225 J. Tian, K. Xu, J. Hu, S. Zhang, G. Cao and G. Shao, *J. Mater. Sci. Technol.*, 2021, **79**, 62–74.

226 H. Ma, Z. Liu, J. Li, Q. Liu, J. Zhang and T. Wei, *J. Alloys Compd.*, 2023, **940**, 168820.

227 L. D. Ellis, A. F. Badel, M. L. Chiang, R. J.-Y. Park and Y.-M. Chiang, *Proc. Natl. Acad. Sci. U. S. A.*, 2020, **117**, 12584–12591.

228 P. Badjatya, A. H. Akca, D. V. Fraga Alvarez, B. Chang, S. Ma, X. Pang, E. Wang, Q. Van Hinsberg, D. V. Esposito and S. Kawashima, *Proc. Natl. Acad. Sci. U. S. A.*, 2022, **119**, e2114680119.

229 B. Singh, A. Goyal, S. Verma, L. Singh and A. Draksharapu, *Sustainable Energy Fuels*, 2024, **8**, 5131–5146.

230 J. N. Bamba, A. T. Dumlaor, R. M. Lazaro, D. D. Matienzo and J. Ocon, *Curr. Opin. Electrochem.*, 2024, **48**, 101592.

231 L. Huang, X. Huang, J. Yan, Y. Liu, H. Jiang, H. Zhang, J. Tang and Q. Liu, *J. Hazard. Mater.*, 2023, **442**, 130024.

232 M. I. Alvarado-Ávila, E. Toledo-Carrillo and J. Dutta, *ACS Omega*, 2022, **7**, 37465–37475.

233 J.-W. Ding, Y.-S. Fu and I.-Y. Lisa Hsieh, *Energy Convers. Manage.: X*, 2024, **24**, 100770.

234 S. Wang, A. Lu and C.-J. Zhong, *Nano Converg.*, 2021, **8**, 4.

235 Wind Speed & Power Generated Dataset For Floating Offshore 7 MW and 15 MW Turbine, [https://data.ncl.ac.uk/articles/dataset/Wind\\_Speed\\_Power\\_Generated\\_Dataset\\_For\\_Floating\\_Offshore\\_7\\_MW\\_and\\_15\\_MW\\_Turbine/24516718/1](https://data.ncl.ac.uk/articles/dataset/Wind_Speed_Power_Generated_Dataset_For_Floating_Offshore_7_MW_and_15_MW_Turbine/24516718/1), (accessed December 19, 2024).



236 Z. Wang, H. Wang, T. Sant, Z. Zhao, R. Cariveau, D. S.-K. Ting, P. Li, T. Zhang and W. Xiong, *Int. J. Hydrogen Energy*, 2024, **71**, 1266–1282.

237 C. A. Rodríguez Castillo, B. Yeter, S. Li, F. Brennan and M. Collu, *Wind Energy Sci.*, 2024, **9**, 533–554.

238 O. S. Ibrahim, A. Singlitico, R. Proskovics, S. McDonagh, C. Desmond and J. D. Murphy, *Renewable Sustainable Energy Rev.*, 2022, **160**, 112310.

239 *Floating Offshore Wind Farms*, ed. L. Castro-Santos and V. Diaz-Casas, Springer International Publishing, *Cham*, 2016.

240 D. Jang, K. Kim, K.-H. Kim and S. Kang, *Energy Convers. Manag.*, 2022, **263**, 115695.

241 A. Rogeau, J. Vieubled, M. De Coatpont, P. Affonso Nobrega, G. Erbs and R. Girard, *Renewable Sustainable Energy Rev.*, 2023, **187**, 113699.

242 China Science Daily Demonstration operation of a 100-kilowatt-level high-efficiency seawater electrolysis hydrogen production system, [https://www.dicp.ac.cn/xwdt/mtcf/202502/t20250217\\_7528001.html](https://www.dicp.ac.cn/xwdt/mtcf/202502/t20250217_7528001.html), (accessed March 25, 2025).

243 Shenzhen University Academician Xie Heping's team: Solving the century-old problem of “direct electrolysis of seawater to produce hydrogen” – China Energy Network, [https://www.cnenergynews.cn/guonei/2023/03/28/detail\\_20230328131624.html](https://www.cnenergynews.cn/guonei/2023/03/28/detail_20230328131624.html), (accessed March 25, 2025).

244 China Classification Society issues AIP certificate for China's first “one-stop offshore green hydrogen, alcohol and ammonia production operation system”, <https://www.ccs.org.cn/ccswz/articleDetail?id=202404070877984720>, (accessed March 25, 2025).

